ELECTROANALYTICAL CHEMISTRY

A SERIES OF ADVANCES

edited by

Allen J. Bard
Department of Chemistry
University of Texas
Austin, Texas

Israel Rubinstein
Department of Materials
and Interfaces
Weizmann Institute of Science
Rehovot, Israel

VOLUME 20

MARCEL DEKKER, INC. NEW YORK • BASEL • HONG KONG

The Library of Congress Cataloged the First Issue of This Title as Follows:

Electroanalytical chemistry: a series of advances, v. 1
New York, M. Dekker, 1996–
v. 23 cm
Editors: 1966–1995 A.J. Bard
1996– A.J. Bard and I. Rubinstein
1. Electromechanical analysis—Addresses, essays, lectures
1. Bard, Allen J., ed.
QD115E499 545.3 66-11287
Library of Congress
0-8247-9996-8 (v. 20)

The publisher offers discounts on this book when ordered in bulk quantities. For more information, write to Special Sales/Professional Marketing at the address below.

This book is printed on acid-free paper.

MARCEL DEKKER, INC.
270 Madison Avenue, New York, New York 10016
http://www.dekker.com

Current printing (last digit):
10 9 8 7 6 5 4 3 2 1

PRINTED IN THE UNITED STATES OF AMERICA

SURFACE PLASMON RESONANCE MEASUREMENTS OF ULTRATHIN ORGANIC FILMS AT ELECTRODE SURFACES

Dennis G. Hanken, Claire E. Jordan, Brian L. Frey, and Robert M. Corn

University of Wisconsin–Madison,
Madison, Wisconsin

I. INTRODUCTION

A variety of surface-sensitive spectroscopic methods are currently employed in the characterization of organic thin films and monolayers at electrochemical interfaces. For example, the techniques of polarization modulation Fourier transform infrared reflection absorption spectroscopy (PM-FTIRRAS) [1–6] electrochemically modulated FTIRRAS [7–9], optical second harmonic generation (SHG) [10–12], IR-visible sum frequency generation [13–16], electroreflectance [17,18], and surface-enhanced Raman scattering [19–21] all possess a degree of surface selectivity or specificity that enhances the spectroscopic signal from the interfacial region. Surface plasmon resonance (SPR) methods are surface-sensitive spectroscopic techniques that employ the enhancement of the optical fields that occur at metal (Au, Ag, Cu, Al) surfaces when surface plasmon polaritons (SPPs) are created at the metal/dielectric interface [22–24].

SPPs are coupled photon-plasmon surface electromagnetic waves that propagate parallel to a metal/dielectric interface. SPPs have been used to enhance the surface sensitivity of a variety of spectroscopic measurements (e.g., one- and two-photon surface fluorescence [25–27], Raman scattering [25,26,28–43], and SHG [44–50]). The intensity of the optical fields associated with an SPP decays exponentially away from the metal surface with a decay length on the order of 200 nm [22,24–26,29,51]. In their simplest form, SPPs can be used to probe the index of refraction and thickness of thin films adsorbed to a metal surface using SPR reflectivity measurements. Ellipsometry is another analytical technique that is sensitive to the thickness and index of refraction of thin films. However, ellipsometry is a less sensitive technique than SPR for ultrathin films (<40 nm, depending on the substrate) [52–54].

SPR reflectivity measurements of film thickness have been used at metal surfaces to study the self-assembly of organic monolayers [55,56], the adsorption of biological molecules [6,57–61], and the formation of ultrathin multilayer films [62–64]. SPR measurements have been used to study electrochemical processes such as surface oxidation and underpotential deposition, and to monitor the potential distribution at an electrode surface [17,65–69]. SPR measurements have also been used in conjunction with scanning force [70], atomic force [71–73], and photon scanning tunneling microscopies [51,74] to provide kinetic and spatial information on interfacial processes.

In this chapter, we present a detailed description of the application of SPR methods to the study of molecular adsorption and ultrathin film structure at gold electrodes. Section II is a brief background section that describes the SPR method in more depth and its application to the study of ultrathin organic films. Section III outlines the SPR experimental parameters, including a description of the apparatus used in our work, and provides several examples of SPR thickness measurements of self-assembled monolayer and multilayer films on gold surfaces. The optical technique of SPR imaging is described in Sec. IV, and some examples of its applications to the study of specific and nonspecific adsorption onto charged gold surfaces are presented. Finally, Sec. V describes a novel extension of the SPR technique, denoted electrochemically modulated surface plasmon resonance (EM-SPR), that can be used to determine the electric field strength and electric field profile within ultrathin organic films at charged gold electrode surfaces.

II. BACKGROUND

SPPs are electromagnetic waves that propagate along the interface between a metal and a dielectric medium. They are created by coupling the energy from photons into oscillating modes of electron density at the metal/dielectric interface [22–24]. SPPs are formed from p-polarized light waves (i.e., light with its electric field vector oriented parallel to the plane of incidence) and have propagation vectors or wave vectors, k_{sp}, that lie in the plane of the metal surface. The field amplitudes associated with SPPs are maximum at the metal-dielectric interface and decay exponentially away from the interface [22,24–26,29,51].

The dispersion relation of the surface plasmons at a metal-dielectric interface is given by [24,75]:

$$\omega = ck_{sp}\sqrt{\left(\frac{1}{\varepsilon_m}\right)+\left(\frac{1}{\varepsilon_a}\right)} \tag{1}$$

where ω is the frequency of the light, c is the speed of light, k_{sp} is the wave vector of the photon, and ε_m and ε_a are the dielectric constants of the metal and dielectric (often air or water). The dispersion relationship for a gold/air interface is plotted in Fig. 1 as the solid line. This curve is calculated from Eq. (1) and is based on the free electron gas model for gold, which approximates the dielectric function of the metal $\varepsilon_m(\omega)$ from the

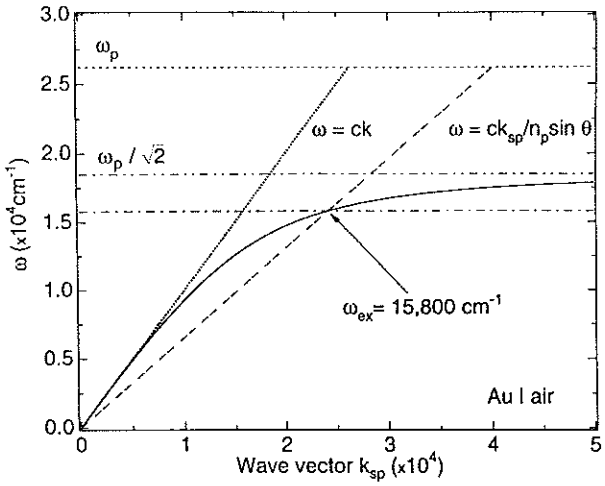

FIG. 1. The dispersion relationship for surface plasmon polaritons (SPPs) at a gold/air interface (solid line). This curve is based on the free electron gas model for gold, which approximates the dielectric function of the metal $\varepsilon_m(\omega)$ from the bulk gold plasmon frequency ω_p (≅26,000 cm^{-1}). The curve approaches an asymptotic frequency called the surface plasmon cut-off frequency $\omega_p/\sqrt{2}$ at ≅18,500 cm^{-1}. Above this frequency surface plasmons cannot be created for this particular interface. The dispersion relation for light propagating in air ($\omega = ck$) and in a prism coupler ($\omega = ck_{sp}/n_p \sin\theta$) are also shown in the figure as the dotted and dashed lines, respectively. Only the prism modified light line intersects with the SPP dispersion curve and can lead to the formation of surface plasmon modes at the gold/air interface (see text).

bulk gold plasmon frequency ω_p (~26,000 cm^{-1}) [75]. The curve approaches an asymptotic frequency denoted as the surface plasmon cut-off frequency $\omega_p/\sqrt{2}$ at ~18,500 cm^{-1}. Above this frequency surface plasmons cannot be created for this particular interface. The dispersion relation for light propagating in air ($\omega = ck$) is also shown in Fig. 1 as the dotted line. The SPP dispersion curve always lies to the right of the light line so that direct excitation by external reflection methods on a smooth metal surface will not couple into the surface plasmon modes. Therefore, it is necessary to use a grating or prism coupling arrangement to excite SPPs [22–24]. For prism coupling, either the Otto or Kretschmann configuration, shown in Fig. 2, can be used [76,77]. The Otto setup requires an air or electrolyte

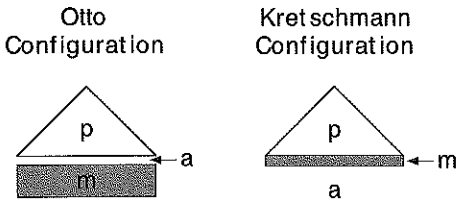

FIG. 2. The two possible coupling configurations to excite surface plasmon polaritons at a metal-dielectric interface. The labels **p**, **m**, and **a** represent a prism, a metal, and a dielectric medium (usually air or water). In the Otto configuration, a thin dielectic medium with a thickness on the order of the wavelength of light is required between the prism and the metal. In the Kretschmann configuration, a thin metal layer with a thickness on the order of the wavelength of light is place in direct contact with the prism. (From Ref. 204.)

gap on the order of the wavelength of light between the prism and the metal. In contrast, the Kretschmann configuration requires a thin metal layer ~50 nm thick that is in direct contact with the prism. In these arrangements, the evanescent light wave produced at the prism/air or prism/metal interface during total internal reflection is coupled into surface plasmon modes at the metal surface due to the increase in the parallel component of the photon's wave vector k_{para} given in the following:

$$k_{\text{para}} = n_p\left(\frac{\omega}{c}\right)\sin\theta \tag{2}$$

where n_p is the index of refraction of the prism and θ is the angle of incidence in the prism. This modified light line is plotted as the dashed line in Fig. 1. This line crosses the SPP dispersion curve at the point labeled ω_{ex}, which is denoted as the excitation frequency and in our experiments corresponds to 15,800 cm^{-1} (632.8 nm). At this point, the momentum matching condition is satisfied ($k_{para} = k_{sp}$), and surface plasmons are created at the gold/air interface. The formation of SPPs is most easily observed as a minimum in a plot of the reflectivity versus incident angle as pictured in Fig. 3. The formation of thin organic films on the metal surface shifts the SPP dispersion curve to larger k_{sp} values, which in turn requires higher incident angles to satisfy the resonance condition of $k_{para} = k_{sp}$. Although most of the work discussed in this review monitors the reflectivity of light at a single wavelength as a function of incident angle in the Kretschmann configura-

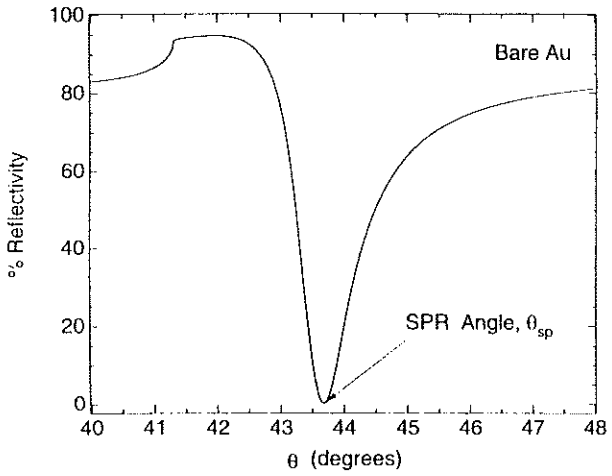

FIG. 3. The formation of surface plasmon polaritons at a gold/air interface. These surface light waves are observed as a minimum in the reflectivity versus incident angle scan. The angular position of this reflectivity minimum is denoted as the SPR angle or θ_{sp}. This curve was obtained from three phase complex Fresnel calculations (see text). (From Ref. 204.)

tion, surface plasmon experiments can also be performed by measuring the reflectivity at a fixed angle as a function of wavelength [78,79]. In addition, several groups have incorporated white light sources or multiple laser wavelengths to monitor reflectivity versus θ scans as a function of wavelength [61,79–86]. This type of arrangement has considerable advantages over single-wavelength scans including the ability to determine both the thickness and index of refraction of a thin film, as long as the film does not absorb over the wavelengths used.

The majority of the initial work using the SPR technique was in the determination of the optical properties of the bare metal and the formation of metal oxide surfaces [22,87]. The application of SPR to the analysis of thin organic films was pioneered in the mid-1970s by Gordon and Swalen [62,88]. This work was expanded to include monolayer films containing highly conjugated dye molecules [80,89,90]. SPR has also been used in electrochemical and other in situ environments to study chemical and physical processes at metal surfaces [17,65–69]. More recently, SPR has been applied to the analysis of thickness and optical properties of LB films

[86,91,92], thin polymer and chromophore-modified polymer films [93–96], and self-assembled monolayer and multilayer films [6,63,64,82,97]. These experimental and theoretical studies have examined the relationship of the optical constants and film thicknesses to the observed SPR reflectivity curves. In addition to measuring thicknesses and optical constants of thin films, the SPR technique has been used to monitor the assembly and reactivity of organic monolayers, photochemical processes, and degradation of thin films [61,72,73,82,95]. Variations of the SPR technique have also been developed to measure nonlinear optical properties of noncentrosymmetric Langmuir-Blodgett multilayers, chromophore-doped polymer films, and self-assembled monolayers [64,91–94,96,98–106].

SPR has also been used extensively to monitor the adsorption of biological molecules onto chemically modified metal surfaces. These studies have been performed on instruments that are generally designed to measure the shift in the SPR minimum to determine an average change in thickness or index of refraction or to produce a spatially resolved image by measuring the percent reflectivity across the surface. These measurements have been done in both ex situ and in situ environments. The ease with which SPR can be performed in situ is extremely advantageous for examining biological samples, which may otherwise denature, and for the investigation of adsorption kinetics [107–111].

The most common SPR instrument measures the average change in thickness or index of refraction caused by adsorption onto a noble metal surface. The metal surface is generally modified to investigate a specific interaction between a molecule immobilized on the surface and some species from solution. Examples of specific interactions that have been studied extensively by SPR include biotin-streptavidin (or avidin) binding [58,97,112,113], antibody-antigen interactions [59,71,114–117], DNA hybridization [61,118,119], and protein adsorption onto silane and alkanethiol self-assembled monolayers [60,120,121]. Supported lipid layers and their interactions with proteins have also been investigated using SPR techniques [122–125].

The in situ SPR reflectivity measurement is the basis of the BIACORE SPR adsorption instrument recently introduced and manufactured by Pharmacia [57]. The sensor chip in this instrument is a gold film coated with a thick (100–200 nm) layer of carboxymethylated dextran. This instrument is sensitive to changes in the index of refraction of the dextran matrix caused by the adsorption of species from solution into the matrix. This has been used for the quantitative detection of numerous biological

species that interact with the dextran or modified-dextran layer [126]. A review of various applications of the BIACORE instrument has been published previously [127].

The technique of SPR imaging has been used to investigate the nonuniform adsorption of a variety of biological molecules onto surfaces [128]. In some cases, the intentional patterning of a sample surface is used to quickly and accurately investigate the adsorption of a molecule onto multiple surface functionalities; for example, the reflectivity from patterned DNA [118] and polypeptide surfaces has been examined using SPR imaging techniques [129]. Alternatively, nonuniform adsorption of molecules onto a surface may be inherent to the sample; for example, SPR imaging has been used to characterize domain formation in supported phospholipid layers [130,131] and antibody-antigen binding within these domains [132].

The popularity of the optical technique of surface plasmon resonance to monitor adsorption processes is rapidly increasing due to its submonolayer sensitivity and experimental simplicity. This section has provided a brief introduction to the various uses of SPR reflectivity measurements; a further description of the work in the literature may be obtained by referring to the cited reviews. A detailed description of three particular instrumental methods that utilize surface plasmon polaritons is provided in the following sections.

III. SPR MEASUREMENTS OF MONOLAYER THICKNESS ON GOLD SURFACES

A. Introduction

Surface plasmon resonance is a very sensitive method of measuring monolayer and multilayer thickness at gold surfaces. The important experimental and theoretical considerations when making such thickness measurements are described in the following section. First, the necessary parameters required to predict and interpret the formation and changes in the SPR reflectivity curves are obtained from theoretical Fresnel calculations. This is followed by an in-depth description of the SPR experimental apparatus for researchers interested in assembling an SPR instrument. The last part of this section provides some recent examples of the use of SPR to monitor self-assembled films on gold surfaces in both ex situ (air) and in situ (aqueous) environments.

In an SPR experiment, the percentage of laser light reflected from a prism/gold film/sample multilayer is monitored as a function of incident angle θ as shown in Fig. 4. The resulting reflectivity curves are modeled with theoretical Fresnel calculations to obtain the thicknesses of ultrathin organic films assembled onto the gold surface. These Fresnel calculations are based on reflection and transmission of light from a one-dimensional multilayer dielectric stack that consists of multiple planar phases. The reflected and transmitted light intensities can be described in terms of the optical constants and thicknesses of the various phases (the first (incident) and last phases are taken to have semi-infinite thicknesses). A number of papers have derived three, four, and N phase reflectivity equations to analyze SPR reflectivity curves [56,79,133–135]. These Fresnel calculations are vital to the analysis and interpretation of the experimentally measured SPR reflectivity data and are particularly useful for predicting changes in

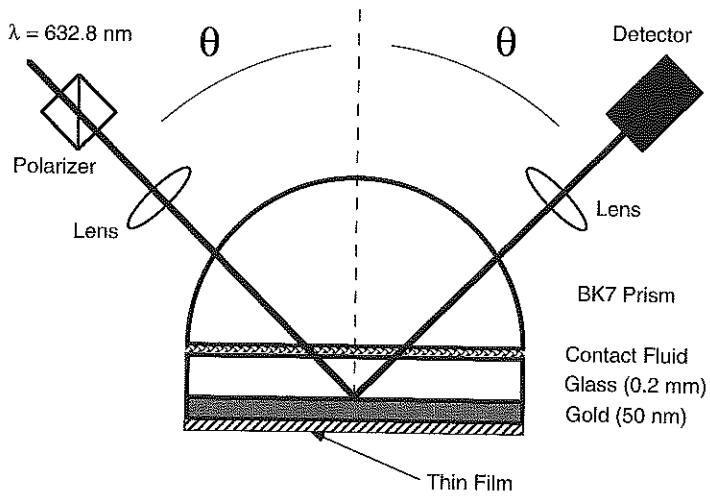

FIG. 4. A view of the prism-gold sample assembly for an SPR instrument. A 50 nm gold film evaporated onto a glass microscope slide cover serves as the substrate for the formation of a thin film. This sample is brought into optical contact with a hemispherical prism in order to couple the laser light into the surface plasmon modes at the gold surface. Rotating the prism-gold sample assembly allows the reflectivity to be recorded as a function of the incident angle, θ. (From Ref. 6.)

SPR reflectivity curves upon ultrathin film formation. In addition, these theoretical calculations are critically important to the design of other SPR experiments.

B. SPR Metal and Dielectric Film Thickness Parameters

Optimization of the optical parameters affecting SPR thickness measurements can be performed through the use of theoretical Fresnel calculations. The SPR experiments described in this review utilize the Kretschmann configuration in which a thin gold film is in direct contact with a glass prism. The thickness of the gold layer is a key parameter for obtaining highly sensitive SPR measurements. Figure 5 displays a series of theoretical Fresnel reflectivity curves calculated for a BK7 glass prism/gold interface as the gold layer thicknesses is varied. The 0 nm curve corresponds to the reflectivity expected for a simple BK7 prism/air

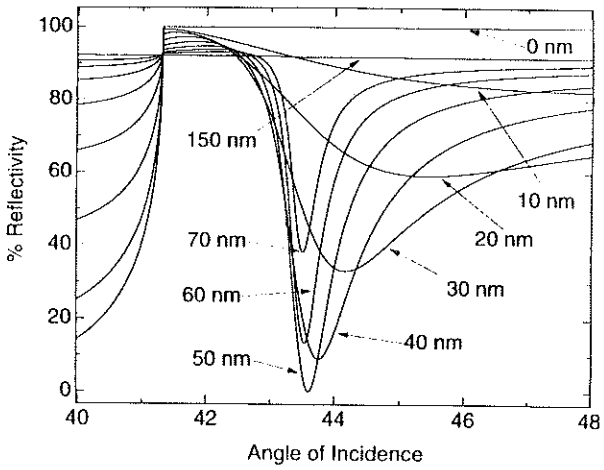

FIG. 5. SPR reflectivity curves for various gold thicknesses determined from complex Fresnel calculations. The curve corresponding to 50 nm of gold on the prism gives the largest drop in reflectivity at the SPR angle, and therefore is the optimal thickness for SPR measurements under these conditions. The following values were used in the calculations and are similar to those determined experimentally: $n_{prism} = 1.515$, $n_{Au} = 0.154 + 3.55i$, $n_{air} = 1$, and the wavelength of light was 632.8 nm. (From Ref. 204.)

interface; notice that total internal reflection (100% reflectivity) is observed at all angles greater than the critical angle (41.3°). As the gold thickness is increased, the reflectivity at angles *less than* the critical angle increases due to some reflection by the gold. At angles *greater than* the critical angle, the reflectivity decreases due to the creation of surface plasmons at the gold/air interface. For thicknesses up to 50 nm, the SPR reflectivity curves get sharper and steeper and eventually have a minimum of 0.1% reflectivity or less. The angle at which this minimum occurs is denoted as the surface plasmon angle θ_{sp}. Above 50 nm, the curves remain sharp, but show less of a decrease in reflectivity at θ_{sp}. Gold films of 150 nm or greater no longer allow coupling of the light into surface plasmon modes and simply show a constant reflectivity of about 92% regardless of the angle of incidence. To obtain the greatest sensitivity from the SPR measurements, a steep drop to nearly 0% reflectivity is desired; therefore, a gold thickness of approximately 50 nm is used. The optimal thickness depends on the optical constants of the gold film, and these can vary depending on the exact deposition conditions of the gold thin film. Fitting the experimental SPR reflectivity curves for each sample to theoretical curves is necssary to obtain accurate thickness results. This need arises from the sample-to-sample variations in the gold layer thickness that occur during the metal deposition step. These gold thickness variations result in different SPR angles for the different clean gold surfaces. For this reason, all of the SPR data are fit to theory curves for each clean gold surface and each successive monolayer.

An example of this fitting process is shown in Fig. 6. This figure graphs the experimental SPR reflectivity curve obtained for a clean gold surface (open circles) and the theoretical fit (solid line) as determined from three-phase (BK7, Au, air) Fresnel calculations. In the fitting routine, three parameters are kept constant ($n_{BK7} = 1.515$ for the prism, $n_{air} = 1.0$, and $\lambda =$ 632.8 nm) and three parameters are varied: the gold layer thickness (d_{Au}) and the real (n_{Au}) and imaginary (k_{Au}) components of the index of refraction. The bulk values for the gold index of refraction ($n_{Au} = 0.166$, $k_{Au} =$ 3.15)[136] may be used as an initial guess for the calculation of the SPR reflectivity curve. First, d_{Au} is adjusted to fit the critical angle region since the percent reflectivity at angles less than the critical angle (near 40°) is determined by the gold thickness rather than total internal reflection of the prism. The second step deals with changing k_{Au} in order to match the theoretical and experimental SPR angles. The third parameter, n_{Au}, is adjusted to give the correct reflectivity past the SPR angle in the 46–48° region. This three-step procedure frequently requires more than one iteration since

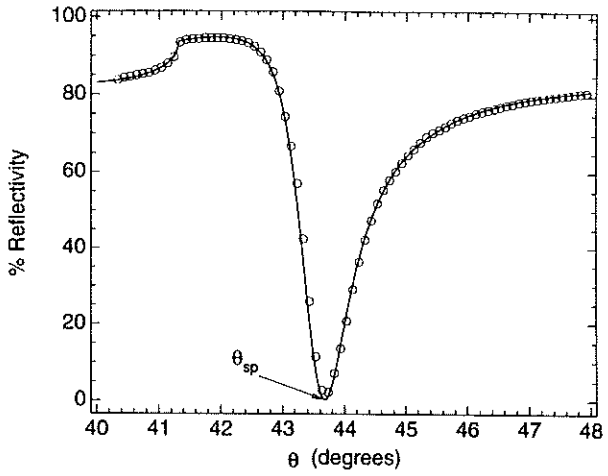

FIG. 6. SPR reflectivity curve for a clean gold surface. The percent of reflected laser light is plotted versus the incident angle, θ. The circles give the experimentally measured values and the solid line is the result of three-phase (BK7, Au, air) complex Fresnel calculations and yield the gold thickness $d_{Au} = 47.0$ nm and index of refraction $n_{Au} + ik_{Au} = 0.163 + i3.52$. The angle of minimum reflection is defined as the SPR angle, θ_{sp}. (From Ref. 204.)

d_{Au}, k_{Au}, and n_{Au} do not act independently on the critical angle region, the SPR angle, and the 46–48° region, respectively. However, these are the regions most affected by each of those parameters. A more complete list of the effects of d_{Au}, k_{Au}, and n_{Au} on the SPR reflectivity curve follows:

Increase in d_{Au}: Increases reflectivity from 40–41°, shifts the SPR angle to a smaller angle, and narrows the SPR curve.

Increase in k_{Au}: Moves SPR angle to smaller angles and significantly narrows the SPR curve.

Increase in n_{Au}: Decreases reflectivity in the 46–48° region and broadens the SPR curve.

Despite the interrelated nature of these parameters, excellent fits to the data result after only two to three iterations. In this example, the theoretical fit corresponds to $d_{Au} = 47.0$ nm and $n_{Au} + ik_{Au} = 0.163 + i3.52$.

The electric field, E, associated with the formation of surface plas-

mons at the gold/air interface, decays exponentially away from the gold surface as shown in Fig. 7. This plot gives E^2/E_o^2 as a function of the distance from the gold surface where E_o^2 is the square of the electric field of the incident radiation. These E^2/E_o^2 values were calculated at the SPR minimum angle of 43.5°. At the gold surface, E^2/E_o^2 is 74, which corresponds to an electric field enhancement of $\sqrt{74} = 8.6$. This enhancement decays exponentially away from the surface and reaches the 1/e value at 164 nm, which gives an estimate of the distance scale probed by surface plasmons. A number of surface spectroscopic techniques have made use of this enhancement including Raman, fluorescence, and second harmonic generation (see Sec. I).

Material adsorbed to the gold surface affects the creation of surface plasmons, which changes the SPR reflectivity curves and allows measurement of an effective thickness of the adsorbed material. Figure 8 plots the SPR reflectivity curves for various thicknesses of adsorbed thin films. The 0 nm curve is simply for a clean gold surface, and the other curves give the

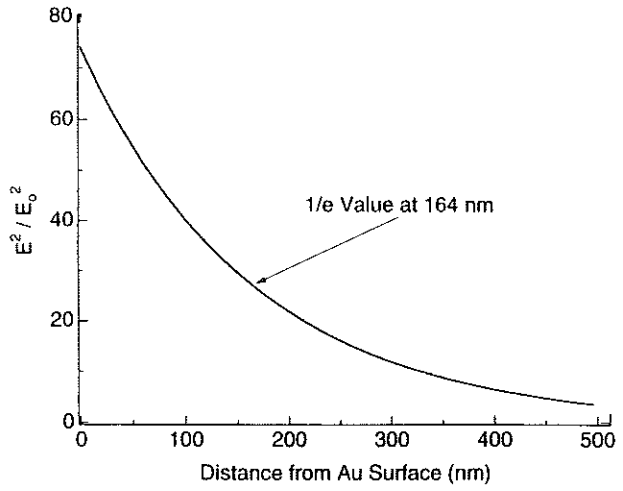

FIG. 7. Electric field strength of the surface plasmon waves as a function of distance from the gold surface. The electric field of the surface plasmons, E, is enhanced over the electric field of the incident radiation. E_o, as shown by the ratio E^2/E_o^2. The electric field strength decays exponentially with distance from the gold surface. (From Ref. 204.)

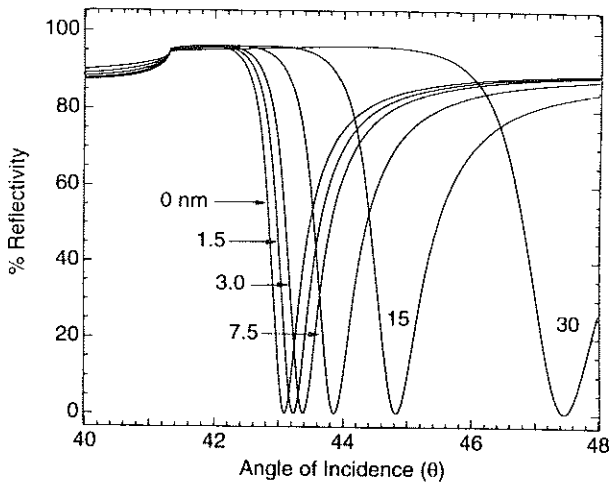

FIG. 8. SPR reflectivity curves for thin films of varying thickness. The 0 nm curve corresponds to that of a clean gold surface. As the film thickness increases, the SPR angle of minimum reflectivity shifts to higher angles and the curve shape becomes significantly broader. These theoretical plots demonstrate that experimental shifts in SPR angle, $\Delta\theta$, can be related to the thickness of material adsorbed to the gold surface, provided the index of refraction is known (in these plots $n_{\text{thin film}} = 1.5$). (From Ref. 204.)

thicknesses in nanometers for thin films with an index of refraction of 1.5. The SPR angle shifts to higher values as more material adsorbs to the gold surface. As the film thickness increases, other changes in the reflectivity curves occur as well. The curves get much broader as seen in Fig. 8. In addition, the percent reflectivity at the minimum increases, but this effect is not easily distinguished in the figure. A plot of $\Delta\theta$ versus the adsorbed layer thickness is shown in Fig. 9 where $\Delta\theta$ is obtained from Fig. 8 by taking the difference in angular position of the SPR minimum reflectivity for the various thickness curves relative to the 0 nm curve. Clearly, the shift in SPR angle as a function of adsorbed layer thickness is nonlinear, and the shift per nanometer is larger for the thicker films.

The shift in the SPR angle not only depends on the thickness of the adsorbed layer, but also upon its index of refraction, n. Figure 10 displays the theoretical reflectivity curves for several 7.5 nm films with different indices of refraction (n = 1.3–1.7). Films with higher values of n

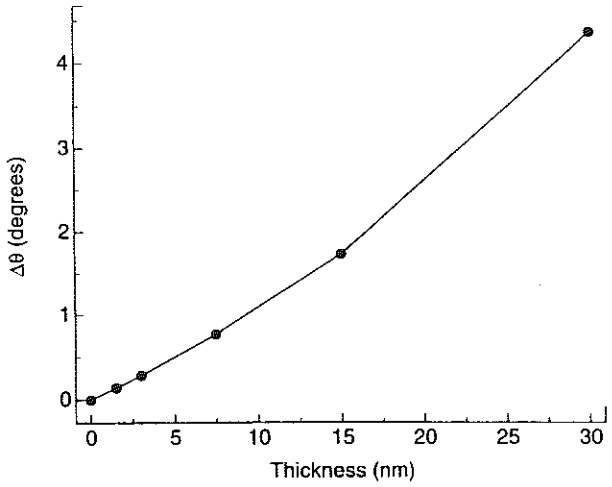

FIG. 9. The shift in SPR angle versus thin film thickness. The values for the shift in SPR angle, $\Delta\theta$, for various thicknesses were obtained from the graph in Fig. 8. Note that a 10 nm thin film gives a shift of over one degree, and that the thicker films give even larger shifts per nanometer. This plot can serve as an approximate conversion of $\Delta\theta$ to thickness for experimental data. (From Ref. 204.)

have larger shifts in the SPR angle, despite having the same film thickness. Note that the indices of refraction used for the film layer in these calculations have only a real component. SPR measurements can be performed on thin films of *absorbing* materials that have an imaginary component to their index of refraction. The conversion of $\Delta\theta$ to thickness then requires a complex index of refraction value. These absorbing thin films also result in broad SPR reflectivity curves that have much higher percent reflectivities at their minima. None of the ultrathin organic films examined in the next sections absorbed light at the experimental wavelength of 632.8 nm, and therefore only the real index of refraction values were required.

In principle, at a single wavelength both the index of refraction and thickness of the monolayer can be extracted from the SPR reflectivity curve by fitting the entire curve rather than just considering the shift in SPR angle. Figure 11 shows two theoretical reflectivity curves that have the same minimum angle but different shapes: the narrower curve is due to

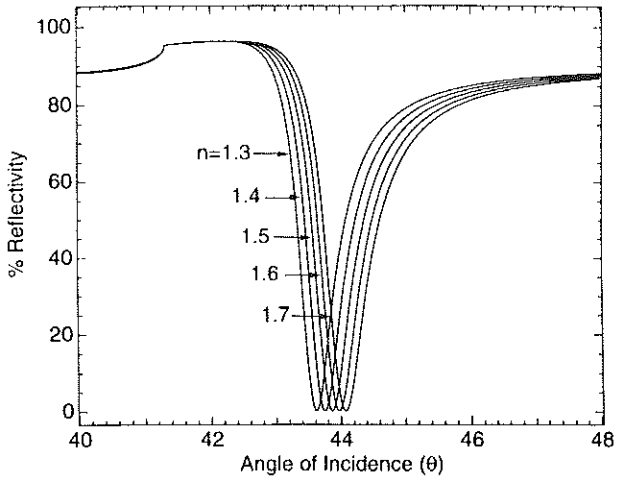

FIG. 10. SPR reflectivity curves for thin films with various indices of refraction. All of these curves correspond to films with a thickness of 7.5 nm, but with different index of refraction values (n = 1.3, 1.4, 1.5, 1.6, and 1.7). Higher index of refraction values produce larger angular shifts. This is similar to that observed for increased film thickness. Therefore, thickness and index of refraction for a thin film cannot be uniquely determined from a $\Delta\theta$ value measured at a single wavelength. (From Ref. 204.)

a film 19.2 nm thick with n = 1.45, whereas the wider curve has a thickness of 15.6 nm and n = 1.60. The inset is an expanded view demonstrating that these films have the same SPR angles. Despite the significant difference in their indices of refraction, these two films give nearly identical SPR reflectivity curves. One could attempt a regression analysis in order to extract both thickness and index of refraction from the experimental data; however, experimental uncertainties such as sample-to-sample variations in the flatness of the gold surface or the uniformity of the thin films have much larger effects on curve shape than the small theoretical difference seen in Fig. 11. Therefore, curve shape alone cannot realistically provide both the thickness and index of refraction for monolayer films [133,134]. However, other researchers have obtained both of these parameters for a monolayer film from SPR experiments made at multiple wavelengths or in different solvents [61,81–86,134,135].

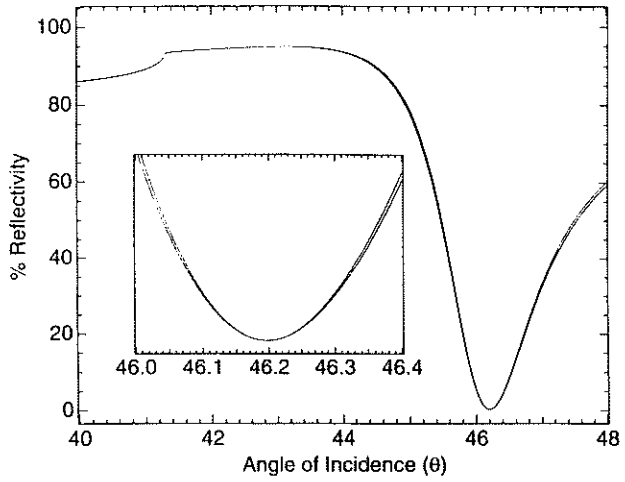

FIG. 11. SPR curves for two films with different thicknesses and indices of refraction, but the same SPR angle. The narrower curve corresponds to a thickness of 19.2 nm and n = 1.45, whereas the broader curve is 15.6 nm thick with n = 1.60. The inset clearly shows that these two films have the same SPR angle of approximately 46.2°. Despite their identical SPR angles, these films have slightly different curve shapes. The experimental curve shape could conceivably provide values for both the thickness and index of refraction for the same film; however, this subtle difference in curve shape is much less than that produced by experimental uncertainties. (From Ref. 204.)

An example of the shift in the surface plasmon angle upon film formation is shown in Fig. 12. This figure plots two experimental surface plasmon reflectivity curves: one is the bare gold curve from Fig. 6 (circles) and the second curve is of the same sample after self-assembly of a monolayer of 11-mercaptoundecanoic acid (MUA) (squares). As mentioned above, a fit to the bare gold film from three-phase Fresnel calculations was used to determine the optical constants and thickness of the gold layer. These values are not changed while determining the thickness of a monolayer film adsorbed to that gold surface using four-phase Fresnel calculations; the only parameters adjusted are the monolayer film thickness (d_{ML}) and index of refraction (n_{ML}). Since it is not possible to determine both d_{ML} and n_{ML} from the same SPR curve at a single wavelength, n_{ML} is usually es-

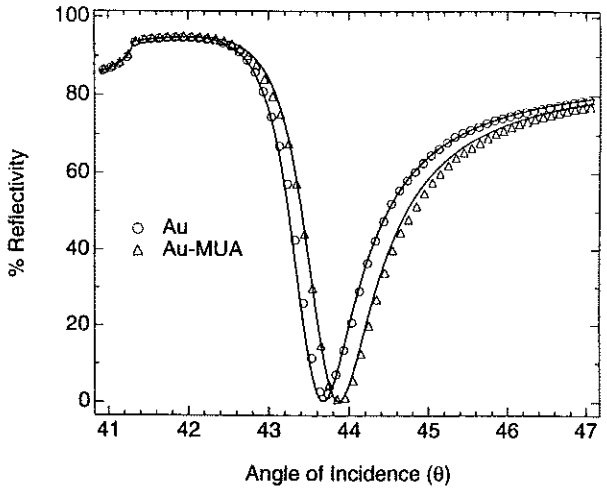

FIG. 12. SPR reflectivity curves for a clean gold surface (circles) and following self-assembly of a monolayer of 11 mercaptoundecanol (MUA) (triangles). The percent of reflected laser light is plotted versus the incident angle, θ. The solid lines are the result of three-phase (BK7, Au, air) and four-phase (BK7, Au, MUA, air) complex Fresnel calculations using the thickness and index of refraction values of gold determined in Fig. 6 of d_{Au} = 47.0 nm and $n_{Au} + ik_{Au}$ = 0.163 + i3.52 and a MUA index of refraction of 1.45. The fit to the MUA SPR curve corresponds to a monolayer thickness of 1.7 nm. (From Ref. 204)

timated from bulk values (which for MUA is about 1.45) or is obtained from another analytical method and then kept constant. The remaining parameter d_{ML} is varied until the theory curve SPR angle exactly matches the experimental SPR angle. The resulting value of d_{ML} is the thickness of the monolayer film, which in the case of the MUA monolayer in Fig. 6 corresponds to 1.7 nm. This process is repeated for each successive monolayer adsorbed to the surface.

The SPR experiments described here focus only on the shift in the SPR angle and its conversion to a thickness value based on an index of refraction, which is estimated, or determined by another analytical method. An error in the thickness calculation is introduced by assuming a value for n rather than measuring it. Similar uncertainties are present in the determination of monolayer and multilayer film thicknesses on metal surfaces

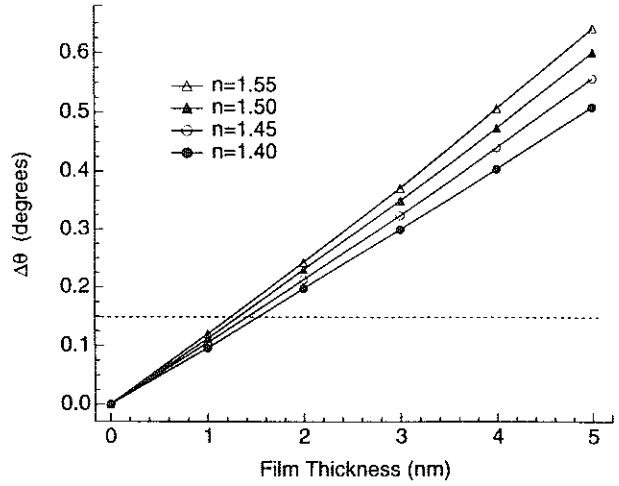

FIG. 13. Calculations of shift in SPR angle versus film thickness for various indices of refraction. The results of a four phase (BK7, Au, film, air) complex Fresnel calculation giving the expected change in SPR angle, $\Delta\theta$, for thin films with thicknesses up to 5.0 nm and different refractive indices: n = 1.40, 1.45, 1.50, and 1.55. The sensitivity of the SPR technique is given by the slope of approximately 0.12°/nm. The dashed line represents a shift of 0.15°, which corresponds to 1.4 nm at n = 1.45. An uncertainly of ±0.05 in the thin film index of refraction gives an error of roughly 0.1 nm for this 1.4 nm film as indicated by the intersections of this dashed line with the solid lines. (From Ref. 6.)

from ellipsometric measurements and have been discussed in the literature [133,137]. To examine the uncertainty caused by estimating n, a four-phase (BK7, Au, film, air) complex Fresnel calculation was performed for a range of values of n. Figure 13 plots the results of these calculations and shows the shift in the SPR angle as a function of film thickness for thin films with n = 1.40, 1.45, 1.50, and 1.55. A variation of ±0.05 in the monolayer index of refraction leads to an error of approximately ±7% (i.e., 0.1 nm for every 1.5 nm of film thickness). Although n may vary somewhat from the bulk index of refraction, it is unlikely to change by more than ±0.05. If the bulk value of n is not known for a given compound, it can usually be estimated within these same limits from the indices of refraction for related compounds.

C. SPR Experimental Apparatus

This section presents a detailed description of the *ex situ* scanning surface plasmon resonance apparatus used in the SPR thickness measurements. The SPR instrument is shown schematically in Fig. 14. The HeNe laser (Newport Corp.) that has a power output of 1 mW, a wavelength of 632.8 nm, and a polarization ratio of 500:1 is used in this setup. To increase the sensitivity, the laser beam is mechanically chopped at a frequency of 930 Hz by a Stanford Research Systems SR540 chopper. Lenses L1 and L2 are employed to collimate the laser beam, which would otherwise diverge and produce too large a spot on the sample. The mirrors M1 and M2 are used

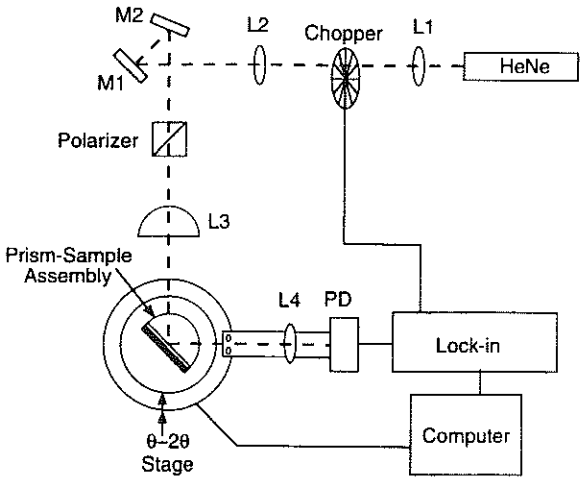

FIG. 14. Overall experimental arrangement for the scanning SPR instrument. Lenses L1 and L2 collimate the HeNe laser beam, and mirrors M1 and M2 are used to align the beam onto the center of the prism-sample assembly. The polarizer is set to p-polarization. The combination of lens L3 (a hemispherical BK7 prism) and the BK7 hemispherical sample prism produces collimated light on the gold sample surface. The incident angle, θ, is changed by rotation of the prism-sample assembly mounted on a θ-2θ stage controlled by a computer with stepper motors. The reflected light is collected using a detector arm, connected to the 2θ part of the stage, which consists of a lens L4 and a photodiode PD. A lock-in amplifier demodulates the chopped signal, and a computer records the reflectivity versus incident angle. (From Ref. 204.)

to align the beam onto the prism-gold sample assembly so that it strikes the gold layer at the center of rotation of the θ–2θ stage in order to avoid walking the beam across the sample during the experiment. A calcite polarizer (Newport Corp) with an extinction ratio of 10^{-5} polarizes the light parallel to the plane of incidence (p-polarization) since s-polarized light does not create surface plasmons. The combination of lens L3 and the hemispherical prism is used to provide a collimated beam impinging on the gold sample. In fact, in order to compensate for the strongly focusing prism, the lens L3 is an identical hemispherical prism placed approximately 2 inches in front of the sample prism. Thus, the laser beam is tightly focused by the prism L3, and then as it diverges the sample hemispherical prism recollimates it to give a narrow range of incident angles on the gold film.

Figure 4 presents an expanded view of the prism-gold sample assembly. The sample consists of a BK7 glass microscope slide cover coated with a thin layer of gold that is subsequently modified with self-assembled monolayer films. The glass substrates prior to gold deposition are rigorously cleaned in concentrated sulfuric acid, rinsed copiously with Millipore water, and then silanized with (3 mercaptopropyl)trimethoxysilane using conditions optimized previously [138].

Gold is vapor deposited onto these substrates using a Balzers vapor deposition apparatus equipped with a turbo molecular pump. The deposition occurs at a pressure of about 1×10^{-6} mbar with around 3.6 amperes running through the tungsten boat containing gold pellets (99.99%) obtained from Canadian gold coins. Gold films of 49 ± 2 nm are deposited at approximately 0.1–0.2 nm/sec by monitoring the thickness with a quartz crystal microbalance (QCM) inside the vacuum chamber. The gold is deposited at room temperature, and the gold/glass samples are subsequently annealed at approximately 300°C for one hour. This procedure results in surfaces with atomically flat Au(111) terraces of about 120 nm in diameter, as determined by STM measurements [6].

The gold-coated samples are brought into optical contact with a BK7 hemispherical prism using an appropriate index matching fluid [ethylene glycol (EG) (n = 1.43), glycerol (n = 1.47), or methyl salicylate (n = 1.53)]. The hemispherical prism ensures that the laser beam is normal to the prism regardless of the angle of incidence. By entering the prism perpendicularly, the beam is not refracted and thus calibration of the incident angle is simplified. Furthermore, the laser spot on the gold surface does not move as the prism-gold sample assembly is rotated.

Therefore, the same spot is sampled throughout the angular scan. Scanning of the incident angle is accomplished by rotating the prism-gold sample combination using a θ–2θ rotation stage assembly with computer-controlled stepper motor drivers that result in an angular resolution of 0.004°.

The entire laser beam that is reflected from the prism-gold sample assembly is collected by lens L4 and focused onto the photodiode PD (Hamamatsu S1336-5BK) (see Fig. 14). The response from the photodiode detector is sent to the lock-in amplifier (Stanford Research Systems SR510) to demodulate the chopped signal. This reflectivity signal is then recorded as a function of incident angle, θ , by a computer, which also controls the stepper motor rotation of the sample and detector.

D. Examples of SPR Thickness Measurements

Three sets of exemplary scanning SPR measurements that monitor monolayer and multilayer adsorption onto a gold surface are presented: (1) Ex situ SPR measurements are used in conjunction with vibrational spectroscopy to monitor electrostatic adsorption of a biopolymer onto a self-assembled monolayer-modified gold surface. These modified surfaces are then used to control protein immobilization. (2) The same combination of techniques is used to monitor the structure and assembly of multilayer zirconium phosphonate (ZP) films having variable indices of refraction. (3) in situ SPR thickness measurements for both biopolymer films and mixed ZP multilayer films are examined.

1. Biopolymer/Protein Adsorption Studies

Through a combination of polarization-modulation Fourier transform infrared reflection-absorption spectroscopy (PM-FTIRRAS) and ex situ SPR measurements, it has been demonstrated that the multiply charged polypeptide poly-L-lysine (PL) will strongly adsorb onto gold surfaces modified with a self-assembled monolayer of 11 mercaptoundecanoic acid (MUA) creating a robust MUA/PL bilayer on the gold surface (see Fig. 15).[6] The PM-FTIRRAS spectroscopic measurements indicate that the PL adsorbs onto the MUA monolayer via the formation of multiple carboxylate-ammonium ion pairs, and that the PL can be released from this surface by rinsing with a buffer solution adjusted to a pH that destroys the ion pairing interactions. In these initial studies it was determined that only a fraction of the PL amino groups participate in the

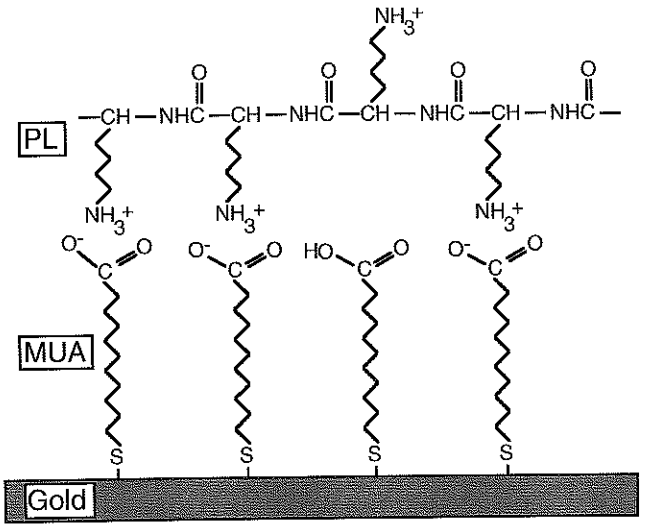

FIG. 15. Schematic diagram of PL and MUA monolayers adsorbed onto a gold substrate. A self-assembled alkanethiol monolayer of 11-mercatoundecanoic acid (MUA) is formed on the gold surface. A monolayer of poly-L-lysine (PL) adsorbs to the MUA coated gold surface via ion pair formation between the ammonium and carboxylate groups. (From Ref. 6.)

electrostatic binding. This leaves a large fraction of the ε-amino groups available to interact with proteins either by direct chemical cross-linking or by specific interaction with chemical functionalities incorporated into the adsorbed PL monolayer.

As an example of controlling protein immobilization onto gold surfaces with PL monolayers, the specific adsorption of the protein avidin was examined in a previous paper [97]. Avidin (MW = 67,000) is a tetrameric glycoprotein that contains four specific binding sites for biotin ($K_{aff} = 10^{15}$ M^{-1}), and the presence of multiple binding sites on the protein has led to its use in numerous biosensor applications [71,139–148]. Avidin and the related protein streptavidin have been absorbed previously onto gold surfaces by specific interactions with surface-immobilized biotin and by simple nonspecific adsorption [59,113,143,149–151].

The approach for the specific adsorption of avidin using PL monolayers is shown schematically in Fig. 16. As discussed above, a self-assem-

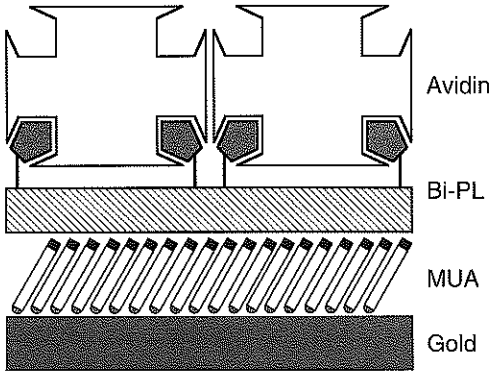

FIG. 16. Schematic diagram showing the specific adsorption of the protein avidin onto a gold surface coated with a biotinylated poly-L-lysine (Bi-PL) monolayer. The Bi-PL is immobilized via ion pair formation with a self-assembled monolayer of 11-mercaptoundecanoic acid (MUA). This diagram is not intended to imply that every avidin is bound to the surface with two biotin moieties. (From Ref. 97.)

bled monolayer of MUA is first prepared on the surface of a vapor-deposited thin gold film. Next, a monolayer of PL in which some of the lysine ε-amino groups have been modified with biotin functionalities (Bi-PL) is electrostatically adsorbed onto the surface. Finally, exposure of this surface to an avidin solution results in the specific adsorption of the protein. To control the surface coverage of avidin, the biotin moieties are attached to the PL prior to its adsorption. This strategy provides for the controlled variation of the percentage of lysine residues that are modified with biotin.

Surfaces with varying numbers of specific adsorption sites for avidin were prepared by chemically modifying PL with different amounts of biotin (0–22% of the lysine residues). These various Bi-PL conjugates were adsorbed electrostatically onto MUA-coated gold surfaces and then exposed to avidin solutions. In this manner, the percent biotinylation of lysine residues needed to produce complete avidin monolayers was determined to be about 20%. The experimental SPR reflectivity curves for the adsorption of monolayers of MUA, 22% Bi-PL, and avidin onto a gold surface are depicted in Fig. 17. The experimentally measured shifts in the SPR angle and the calculated film thicknesses for the various monolayer

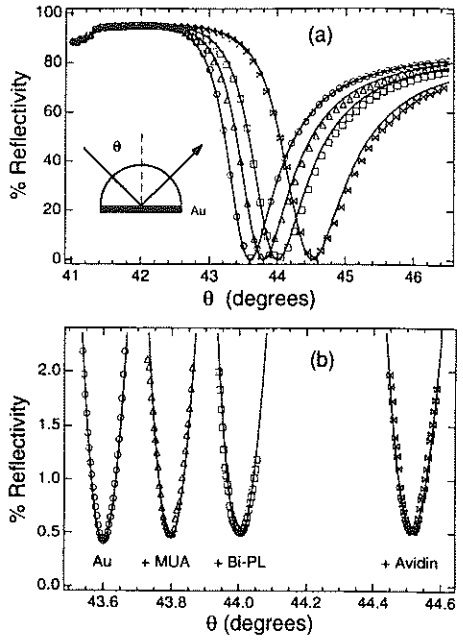

FIG. 17. (a) The SPR reflectivity curves for a clean gold surface (○), and the same surface after the sequential adsorption of a MUA monolayer (Δ), a 22% Bi-PL monolayer (□), and a layer of the protein avidin (■). (b) An expanded view of the SPR curves for the same sample as in (a), but with data points taken every 0.004° to precisely determine the reflectivity minimum also referred to as the SPR angle. The shift in the SPR angle upon adsorption is used to determine the thickness of the adsorbed layer via complex Fresnel calculations (solid lines). (From Ref. 97.)

films are listed in Table 1 (part A). A shift of $\Delta\theta = 0.180 \pm 0.005°$ from the bare surface was observed after the adsorption of the self-assembled MUA monolayer. Using a four-phase (BK7, Au, MUA, air) complex Fresnel calculation, $\Delta\theta$ was converted to a thickness of 1.7 ± 0.1 nm by assuming a MUA index of refraction of $n_{MUA} = 1.45$. This film thickness is in excellent agreement with previous ellipsometric film thickness measurements of 1.6–1.9 nm for the MUA monolayer and confirms the accuracy of the SPR technique [152–154]. A theoretical thickness of about 1.8–1.9 nm is ex-

TABLE 1

SPR Angle Shifts and Calculated Layer Thicknesses

	Layer	Total $\Delta\theta$[a] (degrees)	Additional $\Delta\theta$ (degrees)	Index of refraction[b]	Layer thickness (nm)	Surface coverage[c] (cm^{-2})
Part A	MUA	0.180 ± 0.005	0.180	1.45	1.7 ± 0.1	
	22% Bi-PL	0.385	0.205	1.52	1.7	
	Avidin	0.870	0.485	1.45	4.1	3×10^{12}
Part B	MUA	0.180	0.180	1.45	1.7	
	PL lysines	0.310	0.130	1.52	1.05	4×10^{14}
	Avidin	0.310	0.00	1.45	0	

[a]Total shift in SPR angle from that of the bare gold surface.
[b]Index of refraction estimated from bulk values.
[c]Absolute surface coverage determined from fluorescence measurements.
Source: Ref. 94.

pected for a fully extended MUA monolayer oriented normal to the surface [152,153,155], and so the measured value of 1.7 nm is in agreement with a picture of the MUA molecules forming a close-packed self-assembled monolayer where the methylene chains are oriented nearly perpendicular (i.e., with an average tilt angle of $\leq 30°$) to the surface. The 22% Bi-PL monolayer was adsorbed onto the MUA monolayer from a 5 mM $NaHCO_3$ buffered solution (pH = 8.5). The observed SPR angle shift of 0.205° corresponds to an additiona thickness of 1.7 nm for the 22% Bi-PL monolayer, which is somewhat thicker than a monolayer of unmodified PL (1.05 nm). SPR measurements on monolayers of 0.3–15% Bi-PL gave intermediate thicknesses between the 1.05 and 1.7 nm as expected.

The biotin moieties attached to the surface via the PL acted as specific adsorption sites for avidin. Thus, exposure of the 22% Bi-PL–coated surface to avidin in the same $NaHCO_3$ buffer solution produced an additional shift in SPR angle of nearly 0.5° corresponding to an avidin layer thickness of 4.1 nm, which is in good agreement with the expected thickness for a single monolayer of avidin [59,140,141,143,145,147,149]. Thus, the monolayer thickness of 4.1 nm obtained from the SPR results demonstrates that a complete monolayer of avidin has adsorbed onto the 22% Bi-PL–coated surface. In fact, full monolayers of avidin approximately 4.0 nm thick were also obtained for Bi-PL monolayers with as little as 11% bi-

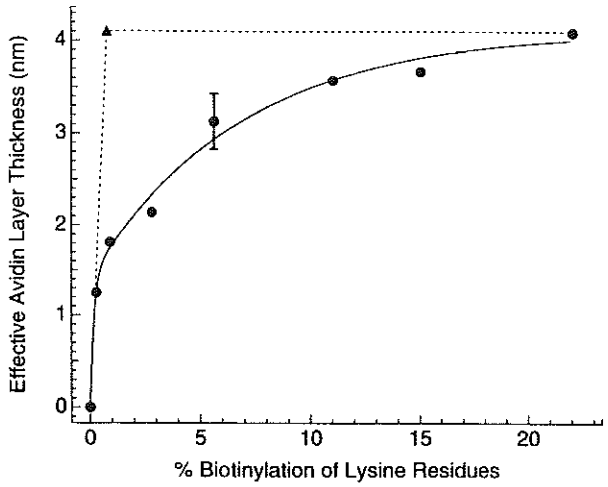

FIG. 18. A plot of effective avidin layer thickness versus the percent biotinylation of the lysine residues of the adsorbed Bi PL. The experimental data points (circles) were determined by SPR thickness measurements and fit with a double exponential (solid line). The calculated curve (dashed line) was obtained via the fluorescence measurements—see discussion in the text. Comparison of the experimental and calculated curves suggests sterically hindered binding of avidin, which could be overcome by increasing the number of specific adsorption sites (i.e., the %Bi-PL). (From Ref. 97.)

otinylation, as shown in Fig. 18. This result agrees with that obtained by Spinke et al., who found that 10% of a biotin-thiol mixed with 90% 11-mercaptoundecanol led to the adsorption of a full streptavidin monolayer [59]. Complete 100% biotin thiol monolayers, however, were observed to hinder streptavidin adsorption and yield lower surface coverages [59,151].

Two control experiments were performed to verify that the avidin was specifically adsorbed onto the biotin sites present on the gold surface. First, SPR measurements determined that no avidin adsorption occurred onto a PL monolayer that had not been biotinylated (Table 1, part B). Second, no avidin adsorption was observed when the Bi-PL–coated surface was exposed to a solution of avidin that had been first saturated with d-biotin. The prevention of nonspecific adsorption of the protein avidin onto the gold surface by the PL (or Bi-PL) monolayers can be ascribed to the

fact that, at the pH of the buffered deposition solutions, both PL and avidin are positively charged. The adsorption of avidin onto charged surfaces was investigated further in the SPR imaging experiments described in Sec. IV.

In addition to the full monolayers of avidin obtained from 11–22% Bi-PL monolayers, partial avidin monolayers could be formed by decreasing the amount of biotin on the PL. The effective avidin layer thickness, which is proportional to surface coverage, was determined with SPR measurements. This avidin layer thickness is plotted in Fig. 18 versus the %Bi-PL. Notice that partial monolayers of avidin resulted from Bi-PL monolayers with less than 11% biotinylation. The %Bi-PL was fixed by the stoichiometry of the one-step solution phase reaction between biotin and the lysine residues of PL *prior* to adsorption of the Bi-PL onto the surface. This method of controlling the spacing of biotin groups on the surface with Bi-PL avoids problems associated with mixed alkanethiol monolayers such as phase segregation [156] and solution composition versus surface composition mismatches [157,158]. This method is also preferable to a surface reaction between biotin and PL already adsorbed to the gold surface, which was found to offer little control, knowledge, or reproducibility of the biotinylation percentage of the PL. The solution phase reaction prior to adsorption, however, provided precise control over the amount of biotin on the gold surface and the resulting avidin coverage.

As seen in Fig. 18, the avidin surface coverage is not a linear function of the %Bi-PL. If all of the biotin moieties in the Bi-PL monolayer were available for binding with avidin, the avidin layer thickness should have increased linearly with the %Bi-PL. Once monolayer (saturation) coverage is reached, no further increase in avidin coverage should be observed. The dashed line in Fig. 18 depicts this "ideal" behavior. The triangle marks the point of saturation (1:1 ratio of biotin and avidin on the surface), which should be 0.75% Bi-PL as determined from fluorescence measurements. The solid line in Fig. 18 is a double exponential fit to the data; several fits were tried, and all gave nearly the same initial slope. This initial slope at low %Bi-PL closely matches the slope expected for "ideal" behavior (dashed line). This agreement indicates that at low surface coverages an avidin molecule binds to virtually every biotin moiety in the Bi-PL monolayer.

At higher %Bi-PL, however, the surface coverage of avidin no longer increases as quickly as expected. This discrepancy is likely due to the sterically hindered binding of avidin; similar steric effects have been

observed previously for biotin-lipid doped Langmuir-Blodgett films on quartz [144]. Once the Bi-PL surface is covered with a significant amount of avidin, avidin molecules from solution have a difficult time finding an adsorption site that is not partially blocked. Nonetheless, at higher %Bi PL (ca. 20%), a large excess of specific adsorption sites is provided, the steric hindrance problem is overcome, and a complete monolayer of avidin is formed.

2. *Zirconium Phosphonate Multilayer Studies*

The combination of PM-FTIRRAS and ex situ SPR measurements has also been used to characterize the structure and assembly of ultrathin multilayer films on gold substrates formed by the zirconium phosphonate (ZP) ligand coupling chemistry first reported by Mallouk and coworkers [63,144,159,160]. These films consist of alternating layers of organic (alkyl or aryl) and inorganic (zirconium phosphonate) structures and are thermally robust and highly reproducible. In this example, ZP multilayers were used to construct ultrathin organic films with both a specific thickness and an index of refraction that could be tuned within a given range ($1.51 \leq n \leq 1.64$ at $\lambda = 632.8$ nm). To accomplish this, ZP multilayer films were formed which contained two different bis(phosphonate) ions: 1,10-decanediylbis(phosphonate) (DBP) and 4,4′ azobis[(*p*-phenylene)methylene]bis(phosphonate) (AZO). As depicted in Fig. 19, monolayers of either DBP or AZO were deposited sequentially onto a substrate primed with a monolayer of phosphorylated 11 mercaptoundecanol (MUD) and one self-assembled monolayer of DBP. For example, a 1:1 AZO/DBP film consisted of alternating self-assembled monolayers of AZO and DBP. By varying the AZO/DBP ratio in the ZP multilayer, the overall index of refraction of the thin film can be controlled.

ZP multilayer films formed from the sequential self-assembly of 20 DBP monolayers onto a primer layer on a gold substrate were examined with a combination of PM-FTIRRAS and ex situ SPR measurements. The positions and relative intensities of the infrared bands did not change with the number of DBP multilayers, indicating that each self-assembled DBP monolayer had an equivalent molecular structure, although the alkyl chains show more disorder compared to long-chain alkanethiol monolayers on gold. The thickness of the DBP multilayer film was determined by a series of ex situ SPR measurements that were performed during the film deposition process. These effects are shown in Fig. 20 during the forma-

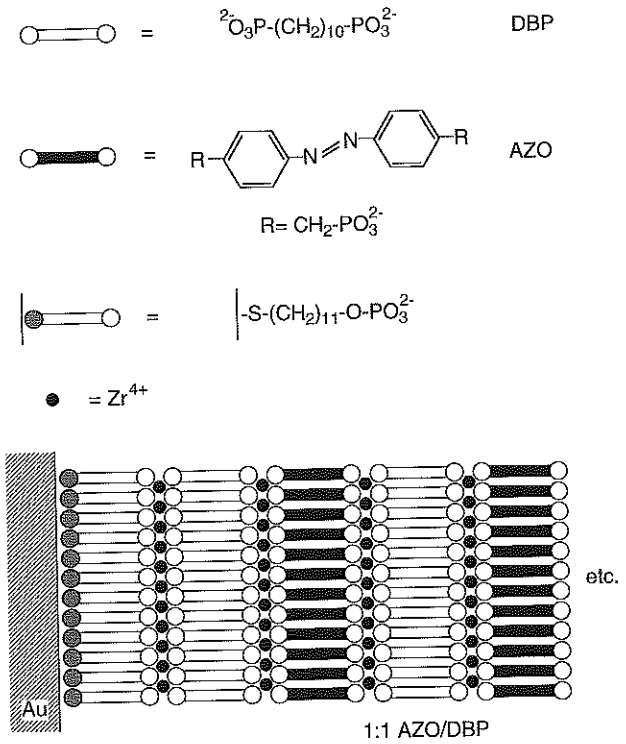

FIG. 19. Schematic diagram for the construction of mixed zirconium phosphonate (ZP) multilayer films. The ZP films are created on vapor-deposited gold substrates that have been first primed with a self-assembled monolayer of phosphorylated 11 mercaptoundecanol (MUD) and one self-assembled monolayer of 1,10 decanediylbis(phosphonate) (DBP). Mixed multilayers are formed by the sequential self-assembly of either 1,10-decanediylbis(phosphonate) (DBP) or 4,4′-azobis [(*p* phenylene)methylene]bis(phosphonate) (AZO) molecules onto the surface. For example, the 1:1 AZO/DBP multilayer film will have alternating self-assembled monolayers of AZO and DBP. (From Ref. 63.)

tion of a multilayer DBP film. Figure 21 plots the shift ($\Delta\theta$) in the SPR angle observed after the addition of each self-assembled monolayer during the formation of a DBP multilayer film relative to the MUD-DBP primer layer.

The shift in the SPR angle observed during the formation of the DBP

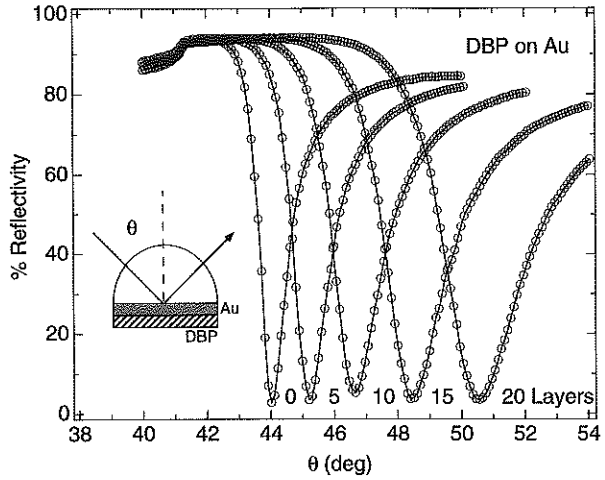

FIG. 20. SPR reflectivity curves obtained during the formation of a 100% DBP multilayer film. These SPR reflectivity curves were taken after the self-assembly of 0, 5, 10, 15, and 20 DBP monolayers. The shifts observed in the SPR angle can be quantitatively related to the thickness and index of refraction of the ZP multilayer. (From Ref. 63.)

multilayer can be used to determine the film thickness (d) if the index of refraction of the film (n) is known. One possibility is to use the bulk index of refraction of n = 1.54; this approach was employed by Mallouk et al. in order to obtain a monolayer thickness of 1.64 nm from ellipsometric data [161]. In principle, ellipsometric measurements of the DBP multilayer on the gold substrate could be used to determine n and d simultaneously; in practice, however, the small shifts in the ellipsometric parameters Δ (the phase difference upon reflection) and Ψ (the arctangent of the amplitude ratio for the s and p components of light upon reflection) observed from monolayers on metal surfaces make this determination difficult [160,162]. An alternate approach employed in this work was to determine n for the various films by ellipsometric measurements on ZP multilayers that had been deposited onto a transparent silica substrate. The primer layer used for the transparent substrates (a bifunctional silane monolayer) was not as well defined as the alkanethiol monolayer employed on the gold substrates and resulted in larger sample to sample variations in film thickness for a

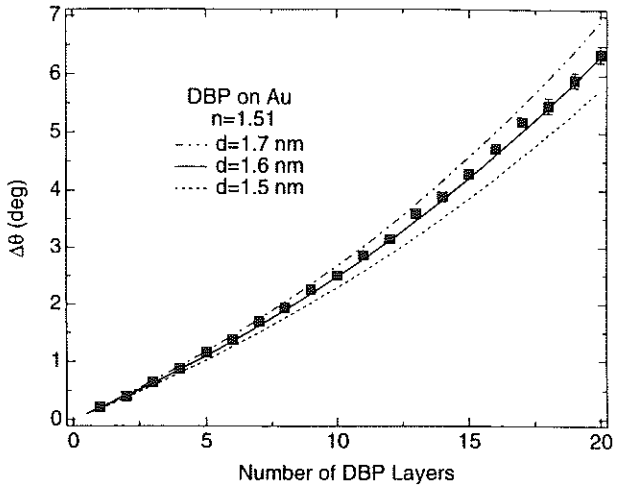

FIG. 21. Shifts in the SPR angle ($\Delta\theta$) measured during the formation of a 20 monolayer 100% DBP film. The shifts $\Delta\theta$ were determined from SPR reflectivity curves such as those shown in Fig. 20 with the SPR angle of the 0 Layer surface defined as $\Delta\theta = 0$. The three lines in the figure are the results of complex Fresnel calculations using an index of refraction of 1.51 (as determined from ellipsometric experiments) for the ZP multilayer and a DBP monolayer thickness of either 1.5, 1.6, or 1.7 nm. From the experimental data a DBP monolayer thickness of 1.6 ± 0.05 nm is determined. (From Ref. 63.)

given number of monolayers. However, for films of 10–30 monolayers, the changes in the ellipsometric parameters Δ and Ψ were large enough to determine the index of refraction to ± 0.01. For example, the Δ and Ψ values for 10, 15, 20, and 25 DBP multilayers deposited onto a silica substrate are plotted in Fig. 22. Also plotted in the figure (the solid and dashed lines) are the theoretical (Δ, Ψ) values expected as a function of film thickness with n fixed at either 1.50, 1.51, or 1.52. The experimental data clearly show that n for the DBP multilayer film is determined to be equal to 1.51 ± 0.01. Similar ellipsometric measurements were used to determine n for the other ZP multilayers described in this paper and are listed along with the value for the 100% DBP film in Table 2.

After determining that the index of refraction for the DBP multilayers is equal to 1.51, the SPR angle shifts in Fig. 21 can be analyzed to as-

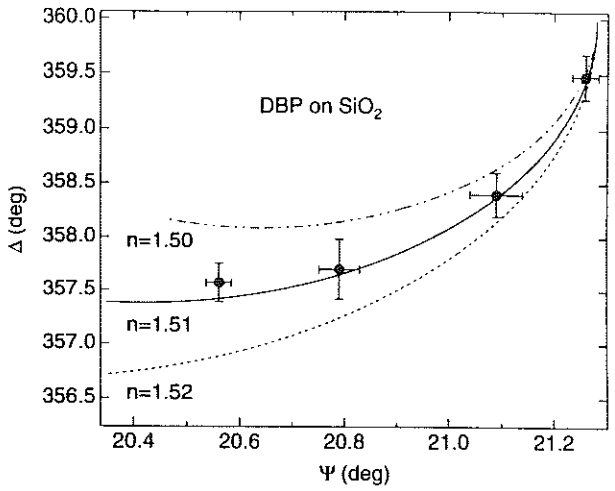

FIG. 22. Ellipsometric measurements for 100% DBP multilayers formed on a fused silica substrate. Values of Δ and ψ after the self-assembly of 10, 15, 20, and 25 DBP monolayers onto the silica surface are plotted as the solid circles in the figure. The three curves in the figure are the results of Fresnel calculations for a three-phase system (SiO_2, film, air) as the film thickness is varied and its index of refraction is set to either 1.50, 1.51, or 1.52. The film thickness for the three curves increases from right to left. From the experimental data, an index of refraction of 1.51 ± 0.01 is obtained for the 100% DBP multilayer. The results of ellipsometric measurements on other ZP multilayers are listed in Table 2. (From Ref. 63.)

TABLE 2

Monolayer Thicknesses and Indices of Refraction for the ZP Multilayer Films

Film	n[a]	d (nm/layer)[b]	$\Delta\theta_{20}$ (deg)	d_{20} (nm)
DBP	1.51 ± 0.01	1.6 ± 0.05	6.36 ± 0.15[c]	32.0 ± 0.5
AZO	1.64	1.6	8.33	32.0
1:1	1.57	1.9	9.65	38.0

[a]Determined by ellipsometry on fused silica substrates.
[b]Determined by SPR on vapor-deposited gold slides.
[c]Reported uncertainty is the standard deviation of three gold-ZP film samples.
Source: Ref. 60.

certain the thickness of the self-assembled DBP monolayers. Using a six-phase Fresnel calculation, the theoretical curves for $\Delta\theta$ as a function of the number of ZP monolayers are plotted in Fig. 21 for monolayer thicknesses of 1.5, 1.6, and 1.7 nm. A comparison of the experimental data points and the theoretical $\Delta\theta$ curves demonstrate that a DBP monolayer thickness of 1.6 ± 0.05 nm can be obtained from the SPR measurements. This thickness agrees favorably with values reported previously [161]. The accuracy of better than ± 0.1 nm is typical for the SPR technique and is remarkable for an optical measurement at $\lambda = 632.8$ nm. Using a space-filling model, the inorganic portion of the DBP monolayer from the center of the first carbon above to the first carbon below the inorganic layer is about 0.65 nm. In an all-*trans* configuration that is oriented perpendicular to the surface, the additional nine methylene groups contribute about 1.14 nm for a total thickness of approximately 1.7–1.8 nm [163,164]. An experimentally determined average monolayer thickness of 1.6 nm is plausible given the possibility of tilting and the presence of alkyl chain disorder in the DBP monolayer as observed in the PM-FTIRRAS spectrum (not shown).

For comparison with the 100% DBP monolayer, a second ZP multilayer was created by the sequential self-assembly of 20 AZO monolayers onto a primer layer on a gold substrate. Again, the positions and relative intensities of the various infrared bands in the PM-FTIRRAS spectrum for the 100% AZO multilayer did not change with film thickness, indicating that each self-assembled AZO monolayer possessed an equivalent molecular structure. As with the DBP film, SPR measurements were performed during the deposition of the AZO multilayer film, and the shift ($\Delta\theta$) in the SPR angle observed after the addition of each self-assembled monolayer is plotted as the squares in Fig. 23. The SPR data for the DBP film from Fig. 21 is also plotted in the figure as the triangles. A larger $\Delta\theta$ per monolayer was observed for the AZO multilayer film; this larger shift is attributed to a higher index of refraction of the AZO multilayer. As listed in Table 2, ellipsometric measurements of AZO multilayer films on a transparent substrate yielded an index of refraction of $n = 1.64 \pm 0.01$. This value is within the range observed for azobenzene-derivatized polymers (1.623–1.758) [165] and is significantly higher than the value of 1.51 observed for the DBP film. Using an index of refraction of 1.64, the six-phase Fresnel calculations can be used to analyze the SPR shifts and determine an average AZO monolayer thickness of 1.6 ± 0.05 nm, which is the same value obtained for the DBP monolayer. Using a space-filling model with an inorganic section thickness of 0.65 nm, the AZO monolayer in which the

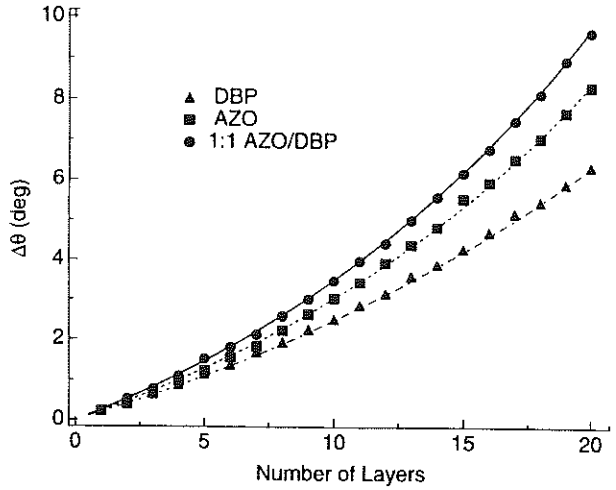

FIG. 23. Shifts in the SPR angle ($\Delta\theta$) measured during the formation of 20 monolayer ZP films of 100% DBP (triangles), 100% AZO (squares), and 1:1 AZO/DBP (circles). The shifts in $\Delta\theta$ were determined from SPR reflectivity curves with $\Delta\theta = 0$ defined as the SPR angle for the primed gold surface (see text for details). The solid and dashed lines are the results of complex Fresnel calculations using the indices of refraction and average monolayer thicknesses for DBP, AZO, and 1:1 AZO/DBP films listed in Table 2. An unexpectedly large average monolayer thickness of 1.9 nm is observed for the 1:1 AZO/DBP film. (From Ref. 63.)

azobenzene is oriented perpendicular to the surface (0.9–1.0 nm) should have a total thickness of approximately 1.7–1.8 nm [163,164]. The smaller experimentally determined value of 1.6 nm again suggests tilting and disorder in the AZO film.

The similarity of the DBP and AZO thicknesses suggests that mixed monolayers of these two molecules may yield stable ZP multilayer films possessing an intermediate index of refraction. Having determined that a DBP multilayer film has an index of refraction n = 1.51 and that an AZO multilayer film has an index of refraction n = 1.64, one would expect that a ZP multilayer film formed from alternating self-assembled monolayers of AZO and DBP would possess an index of refraction of n = (1.64 + 1.51)/2 = 1.575. Indeed, the ellipsometric measurements of a 1:1 AZO/DBP multilayer film on a transparent substrate yield a value of n = 1.57 (see Table 2).

However, SPR measurements on the 1:1 AZO/DBP multilayer suggest that even though n = 1.57 as expected, the structure and thickness of the ZP film has changed. As with the previous two ZP films, SPR measurements were performed during the deposition of the 1:1 AZO/DBP multilayer film in order to determine the average monolayer thickness. The shift $\Delta\theta$ observed after the addition of each self-assembled monolayer is plotted as the circles in Fig. 23 along with the data from the DBP and AZO multilayers. Given that n = 1.57 for this film, one would expect that the $\Delta\theta$ curve for this film would fall in between the curves for the AZO and DBP multilayers. Unexpectedly, the data for the 1:1 AZO/DBP multilayer systematically shows a *larger* $\Delta\theta$ shift than either of the other two films. Using n = 1.57, this $\Delta\theta$ curve corresponds to an average monolayer thickness of 1.9 nm, which is a 19% increase in the average thickness as compared to the 1.6 nm obtained for both the AZO and DBP monolayers. To demonstrate how unusual this number is, if the monolayer thickness is fixed at 1.6 nm, the $\Delta\theta$ curve for the 1:1 AZO/DBP multilayer can only be fit using an index of refraction of 1.70, which is clearly an unreasonable number given n = 1.64 for the 100% AZO multilayer. The uniform shift in the SPR angle for each additional monolayer and PM-FTIRRAS spectra indicate that this 19% increase in thickness results from the incorporation of 19% more DBP in the 1:1 AZO/DBP film than the amount suggested in the simple picture in Fig. 19. The additional DBP could be incorporated into the 1:1 AZO/DBP multilayer film by increasing the packing density within the mixed monolayers and/or by intercalation into the preceding AZO regions of the film.

3. *In Situ SPR Studies*

The two sets of SPR thickness measurements discussed in Sec. III.D.1 and III.D.2 were made in an ex situ environment (air). A major advantage of the SPR technique is that it can be easily modified to monitor monolayer and multilayer film assembly and thickness in an in situ or an electrochemical environment (usually aqueous, but other organic solvents can also be used). This allows for the real-time monitoring of the self-assembly, adsorption, and reaction kinetics of ultrathin films. Since direct optical access to the metal/liquid interface is not required to follow the formation of surface plasmons, in situ SPR measurements require only minor modification of the prism/gold sample assembly to incorporate an in situ flow cell or electrochemical cell.

In addition to an in situ cell, a small number of experimental changes

are also required in moving to an in situ environment. Since the bulk medium of water has a larger optical index of refraction as compared to air (n_{H_2O} = 1.33 at 632.8 nm), the surface plasmon angle shifts to a higher incident angle (>70°) for a BK7 prism/gold sample combination. One method of compensating for this increase in the bulk medium's index of refraction is to use a higher index of refraction prism/gold sample system such as sapphire (n = 1.75) or SF10 glass (n = 1.72). For the in situ SPR measurements shown in this chapter, either SF10 hemispherical prisms or 60° prisms are coupled to gold-coated SF10 microscope slide covers using an index matching fluid (1-iodonapthalene or Cargill n = 1.725 immersion fluid). The in situ surface plasmon angle for the SF10 prism/gold sample system occurs at significantly lower incident angles (~57°) than for the BK7/gold/water case.

Figure 24 plots the in situ SPR curves for a bare gold surface (open triangles) and after modification with a self-assembled monolayer of MUA and

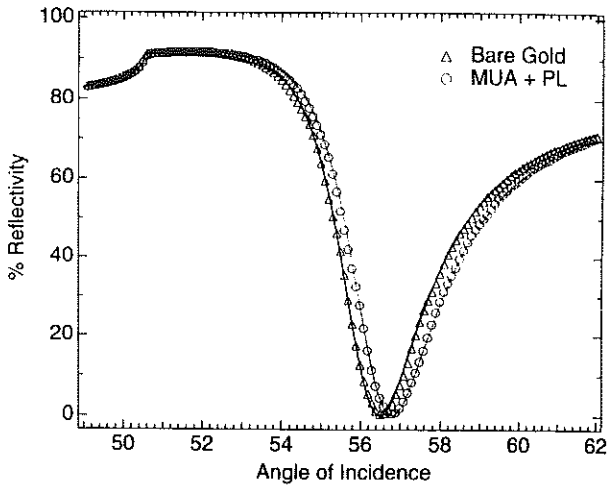

FIG. 24. In situ scanning SPR reflectivity curves obtained for a bare gold substrate (open squares) and the same substrate following self-assembly of a bilayer of MUA and poly-L-lysine (open circles). The curve is the measured reflectivity (%R) of p-polarized light at 632.8 nm from the hemispherical SF10 prism/Au/film/water interface as a function of incident angle, θ. The solid lines in the figure are a five-phase Fresnel fit to the SPR data (see text).

an electrostatically adsorbed poly-L-lysine monolayer (open circles). The SPR angles for these curves are shifted to higher incident angles relative to the corresponding ex situ curves. In addition, the SPR reflectivity curves are broader than the ex situ data. The solid lines are five-phase Fresnel calculations which are fit to the SPR reflectivity data using the previously determined indices of refraction for MUA and poly L-lysine. The thicknesses determined for the MUA and poly-L lysine layers from these Fresnel calculations are 1.6 and 1.3 nm, respectively. These in situ results are in good agreement with those determined ex situ in Sec. III.D.1 (see Table 1). The slight increase in the PL monolayer thickness measured in situ may possibly be due to hydration of the PL monolayer in the aqueous environment.

In situ SPR measurements have also been used to determine the thicknesses of mixed ZP films of DBP and the nonlinear optical molecule HAPA ([5-[4-[[4-[(6-hydroxyhexyl)sulfonyl]phenyl]azo]phenyl] pentoxy]-phosphonic acid). These mixed ZP films of DBP and HAPA are used in Sec. V to measure the electric field profile within multilayer films at charged gold electrodes. In the in situ SPR measurements shown in Fig. 25, the reflectivity (%R) of a p-polarized HeNe laser was monitored as a function of the incident angle (θ) for a 60° SF10 prism/gold/ZP film/electrolyte interface. The ZP film in this experiment consisted of a phosphorylated MUD primer monolayer, one HAPA ZP monolayer, and one DHP (dihexadecylphosphate) monolayer (see Sec. V.C for details). The solid line in Fig. 25 is a five-phase Fresnel calculation using index of refraction n_{DBP} and n_{HAPA} values determined previously [64] and an overall thickness d of 6.7 nm as measured from ex situ scanning SPR experiments. The inset graph in Fig. 25 plots the angular shift in θ_{sp} relative to a single HAPA monolayer film with increasing DBP overlayers. The solid line in the inset is a seven phase Fresnel fit to the data, again using previously determined values n_{DBP} and n_{HAPA}, and corresponds to an increase in the ZP film thickness of 1.6 ± 0.2 nm per DBP monolayer. This DBP layer spacing is equivalent to that measured for pure multilayer DBP films in the ex situ experiments descried in Sec. III.D.2.

The SPR data described in this section and PM-FTIRRAS experiments presented previously [6,63] demonstrate that the optical techniques of surface plasmon resonance and PM-FTIRRAS are a powerful combination of methods for the determination of monolayer and multilayer film thickness and structure. The scanning SPR technique has the additional advantage that it can be easily adapted to monitor film formation and adsorption processes in electrochemical, biological, and other in situ environments. Additional in

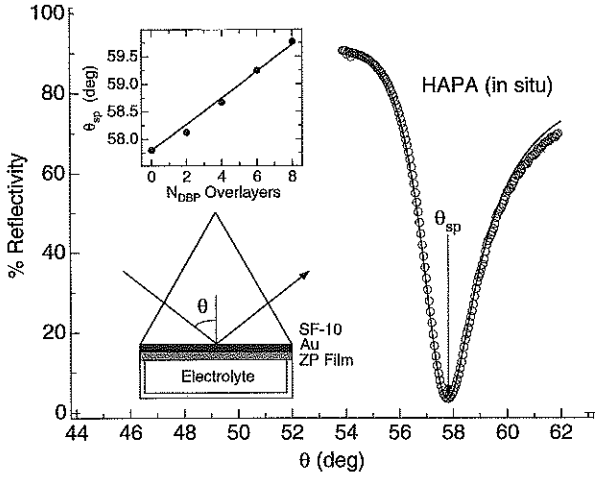

FIG. 25. In situ scanning SPR reflectivity curve obtained for a ZP film that consisted of a phosphorylated MUD primer layer, one HAPA monolayer, and one DHP capping monolayer on a gold substrate (open circles). The curve is the measured reflectivity (%R) of p-polarized light at 632.8 nm from the 60° SF10 prism/Au/ZP film/electrolyte interface as a function of incident angle, θ. The solid line in the figure is a five-phase Fresnel fit to the SPR data (see text). The inset graph follows the shift in θ_{sp} upon the formation of N DBP monolayers where N varied from 0 to 8. The solid line in the inset graph is a seven phase Fresnel fit to the data and yields the average ZP film thickness (see text). (From Ref. 105.)

situ SPR methods for studying multilayer organic film formation on gold surfaces are detailed in the next two sections.

IV. SPR IMAGING EXPERIMENTS

A. Introduction

Along with the scanning SPR technique described in the previous section, fixed angle SPR imaging can also be employed to measure adsorption onto patterned alkanethiol self-assembled monolayers. SPR imaging and microscopy have been used previously by various researchers to study adsorption onto patterned surfaces [128,131,132]. The ability of the SPR imaging technique to observe patterned surfaces is useful when it is desir-

able to monitor adsorption onto many surface functionalities simultaneously, as required in many biosensor applications. For example, SPR imaging allows differential biopolymer adsorption studies to be performed very accurately because two functionalized surfaces can be placed on the same substrate and exposed to identical conditions.

A schematic diagram of the SPR imaging apparatus is shown in Fig. 26. In this experiment, an expanded HeNe laser beam is incident on the prism/thin gold film sample assembly near the SPR angle, and the reflected light is detected with an inexpensive CCD camera to produce images such

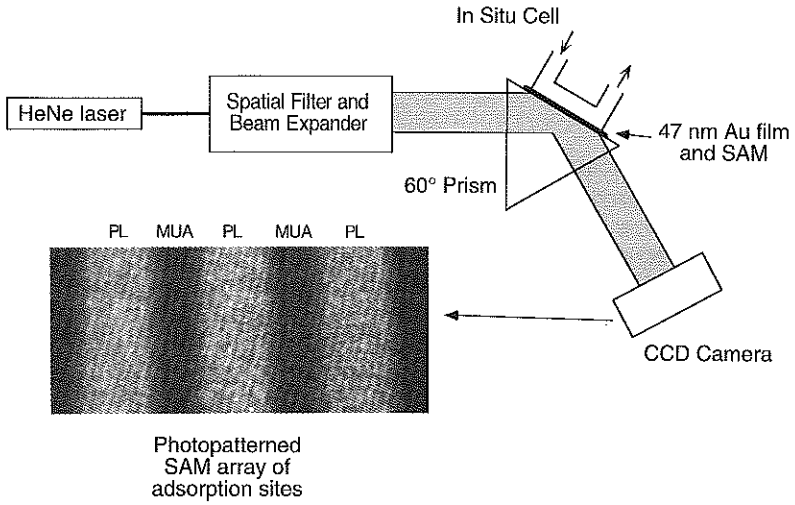

FIG. 26. Optical layout for the SPR imaging instrument. A HeNe laser is sent through a spatial filter and beam expander, which are required so that the entire sample surface can be illuminated. This expanded beam is then directed at the prism sample assembly. A 47 nm thick gold film vapor deposited onto a glass slide is used as the sample substrate for the formation of patterned self-assembled monolayer (SAM) films. This is in contact with a 60° prism which is required to couple the incident p-polarized light into the surface plasmon modes at the interface. In the imaging setup the reflected intensity, at some fixed angle, is then measured across the beam using a CCD camera. For in situ experiments a flow cell is attached to the back of the prism sample assembly so that the gold sample is in contact with solution. An image of a photopatterned SAM array obtained with this instrument is also shown in the figure. (From Ref. 129.)

as those shown in the figure. Any change in the index of refraction or the thickness of a film adsorbed to the gold surface results in a change in the intensity of the reflected light observed at a fixed angle. By creating two different alkanethiol self-assembled monolayers (SAMs) with UV photopatterning on a single thin gold film, a differential adsorption measurement can be performed by monitoring changes in the SPR image as the sample is exposed to a solution of interest. These differential adsorption measurements are equal in sensitivity to the SPR angle shift measurements of biopolymer adsorption performed previously with the scanning SPR instrument. The SPR imaging technique can be used to monitor the adsorption of submonolayer amounts of material in both ex situ and in situ configurations. The following examples demonstrate the use of SPR imaging to characterize the adsorption of proteins, polypeptides, and oligonucleotides onto modified gold surfaces.

B. Ex Situ SPR Imaging Experiments of Biopolymer Adsorption

SPR imaging experiments are performed in our laboratory at a single fixed angle to monitor differences in biopolymer adsorption onto photopatterned chemically modified gold surfaces. For example, a negatively charged MUA monolayer can be used to electrostatically adsorb the polycation poly-L-lysine or any positively charged protein such as avidin (see Fig. 27). One method of determining the difference in thickness between the PL monolayers and the avidin monolayers formed by this electrostatic adsorption process is to measure the different SPR angle shifts obtained from ex situ scanning SPR experiments, as described in the previous section. Figure 28a plots the experimental and theoretical SPR curves for a PL monolayer and an avidin monolayer formed on a negatively charged MUA surface. The circles in the figure correspond to the experimental SPR curve obtained from a PL monolayer, and the squares are the experimental data from an avidin monolayer. In addition to the SPR angle shift, the change in %R at a fixed angle near the SPR minimum can be used to quantitate the difference in thickness between the two monolayers. Figure 28b plots the differential percent reflectivity (Δ%R) curve, which is simply the difference in the two observed percent reflectivities (%R) as a function of incident angle. A maximum in the differential reflectivity is observed just below the SPR angle; SPR imaging experiments are typically performed at this angle to obtain the highest sensitivity to changes in the thickness or index of refraction of the adsorbed material.

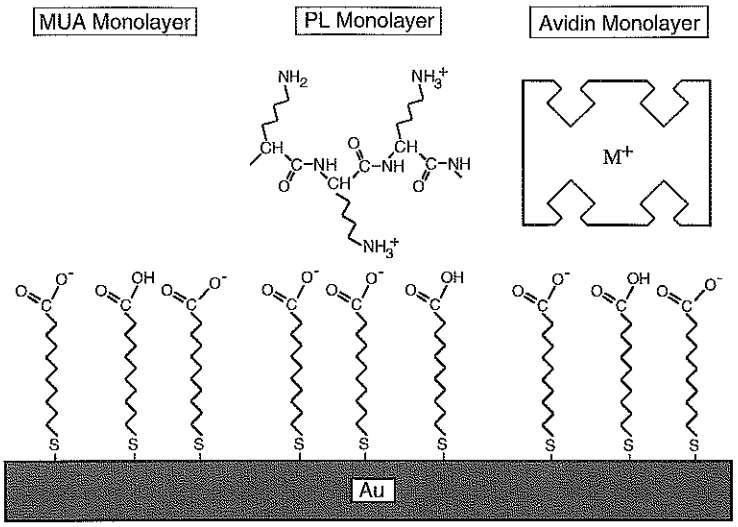

FIG. 27. A schematic diagram of three monolayers adsorbed onto a gold substrate: a negatively charged 11 mercaptoundecanoic acid (MUA) monolayer, a positively charged poly L-lysine (PL) monolayer electrostatically adsorbed to MUA, and the protein avidin electrostatically adsorbed to MUA. (From Ref. 129.)

In order to make differential adsorption measurements with the SPR imaging apparatus, two-component surfaces are created that consist of alternating stripes of two different surface functional groups. These surfaces are prepared by a series of adsorption/self-assembly, photochemical desorption, and rinsing steps. For example, the procedure required for the formation of surfaces with stripes of both PL and MUA monolayers (MUA-PL surface), used for all protein differential adsorption experiments, is shown in Fig. 29. First, a SAM of MUA was formed on a gold surface after which PL was electrostatically adsorbed onto the MUA as described previously [6]. After formation of the PL/MUA bilayer, the surface was placed behind a mask and irradiated with UV light. The UV irradiation causes the gold thiolate bond to be oxidized [166–168] so that both the MUA and PL layers are removed from the exposed stripes by rinsing with ethanol and water. This photopatterned surface is then re-exposed to an ethanolic MUA solution, resulting in a surface with alternating regions

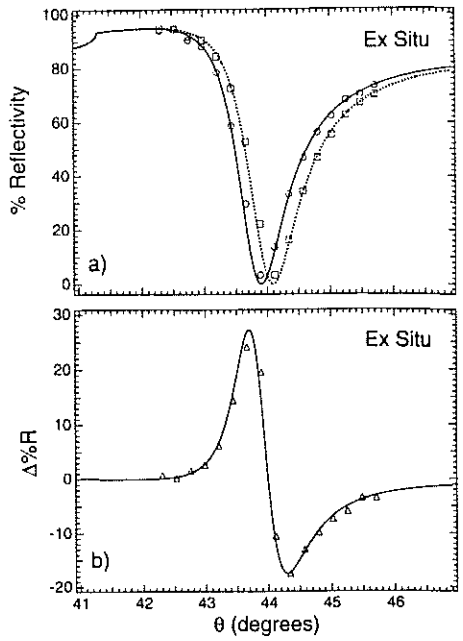

FIG. 28. SPR reflectivity and differential reflectivity curves for PL and avidin monolayers measured ex situ. (a) Experimental and theoretical SPR reflectivity curves for PL and avidin surfaces. The circles and squares show, respectively, the experimental % reflectivities for PL and avidin monolayers measured as a function of incident angle, θ. The solid and dotted lines are the result of four phase complex Fresnel calculations for PL and avidin films and the shift in the angle of minimum %R is due to the difference in thickness between the two monolayers. (b) The experimental and theoretical differential reflectivity curves obtained from the difference in the SPR curves in (a) for PL and avidin monolayers. (From Ref. 129.)

of MUA and PL monolayers. At a neutral or slightly basic pH, the areas of PL will be positively charged and those of MUA will be negatively charged; this surface can thus be used to examine the electrostatic adsorption of proteins. When the reflectivity from such a surface is measured in an SPR imaging experiment at a fixed angle, images of the type shown in Fig. 26 are obtained. The %R values for images are obtained by taking a ratio of the intensity of images observed using p- and s-polarized incident

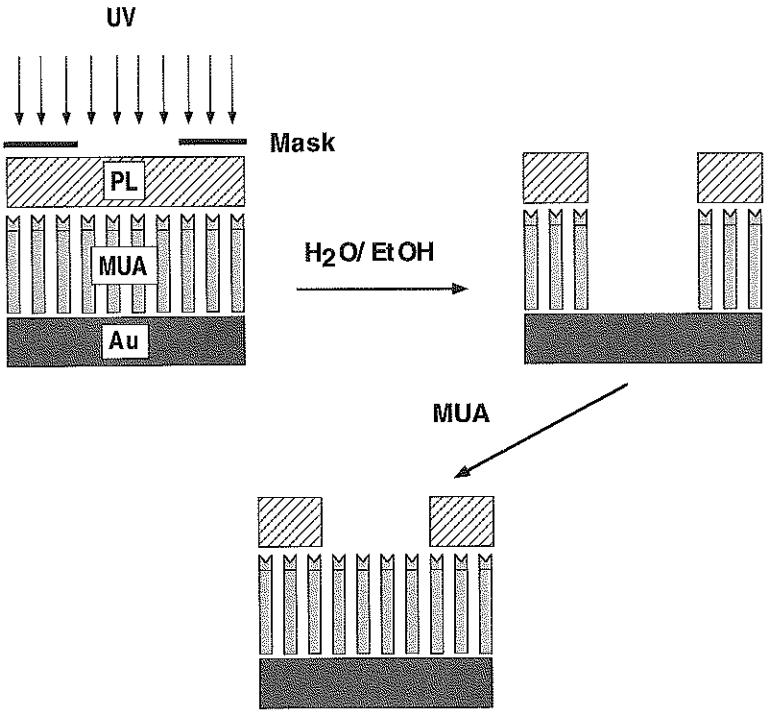

FIG. 29. Schematic diagram outlining the process for making patterned MUA and PL surfaces. Initially MUA is adsorbed onto the gold surface from an ethanolic solution and PL is electrostatically bound to the MUA. This PL monolayer is then placed behind a mask and exposed to UV light. The UV light oxidizes the gold sulfur bond so that both the MUA and the PL can be removed in the exposed areas by rinsing with water and ethanol. MUA can then be readsorbed to the exposed gold creating a surface containing areas of MUA and areas of PL, which is used to study differential protein adsorption. (From Ref. 129.)

light. These images are represented quantitatively by averaging the %R values measured at each pixel of the CCD camera along the stripes and generating a "line profile" across the image.

For example, line profiles generated from SPR images of two MUA-PL surfaces are plotted as the solid lines in Fig. 30. The SPR images were obtained at an incident angle below the SPR angle, and the line profiles

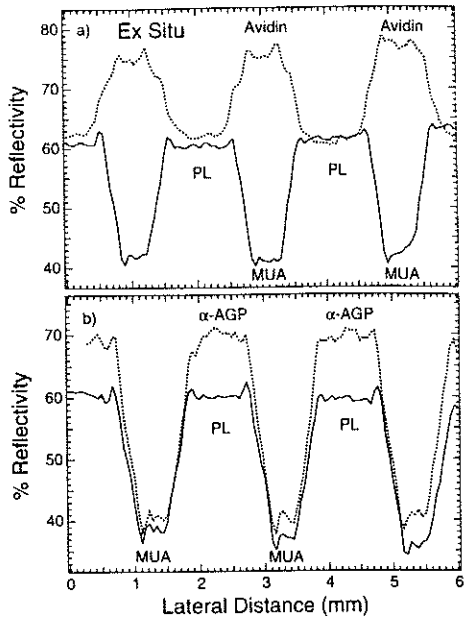

FIG. 30. Line profiles showing the adsorption of avidin and α-acid glycoprotein onto patterned MUA PL surfaces. The solid lines in both (a) and (b) are the % reflectivities measured for gold samples photopatterned with stripes of PL and MUA. The dotted line in (a) is the %R measured after exposing the sample to a pH 8.5 avidin solution and subsequent rinsing with water. The adsorption of α-AGP at pH 8.5 onto a MUA-PL sample is shown by the dotted line in (b). (From Ref. 129.)

from these images show that the %R from the PL monolayer is higher than the MUA monolayer as expected since it is thicker by 10.5 Å [6]. This surface should contain both negatively charged MUA regions and positively charged PL regions when exposed to an aqueous solution of pH 8. The dotted lines in Fig. 30 are the line profiles for two such surfaces that have been exposed to solutions of either avidin (isoelectric point (pI) = 10) or α-acid glycoprotein (α AGP, pI = 3). The surfaces have been removed from the adsorption solution and rinsed with a buffer solution before being imaged. From these ex situ measurements, it is evident that the avidin nonspecifically binds to the MUA regions of the surface, and the α-acid glycoprotein nonspecifically binds to the PL regions of the surface. Thus,

the nonspecific adsorption of these two proteins appears to be dominated by the electrostatic interactions between the proteins and the surface functional groups.

While in principle this information could have been obtained from a series of scanning SPR measurements, the SPR imaging technique is a rapid and very sensitive method for studying protein adsorption. The speed and sensitivity of these experiments arise from the fact that adsorption onto a single surface containing multiple areas with different functional groups can be measured simultaneously and that each functional group is exposed to identical adsorption conditions. Very small changes in %R corresponding to submonolayer amounts of biopolymer adsorption can be observed with this measurement, and if the data are normalized (as in Fig. 30) to obtain quantitative %R values, an effective average thickness can be determined.

C. In Situ SPR Imaging Experiments of Biopolymer Adsorption

1. Avidin Adsorption onto Patterned MUA/PL Surfaces

The same SPR imaging experiments that were performed ex situ on the adsorption of avidin onto MUA-PL surfaces can also be performed in situ with the photopatterned monolayers in contact with an avidin adsorption solution. The in situ SPR imaging differential adsorption measurements are employed to examine how the isoelectric point of a protein, the solution pH, and the electrolyte concentration can affect the electrostatic adsorption of proteins onto a chemically modified gold surface. As in the previous section, a comparison of the SPR curves obtained from in situ scanning SPR measurements for PL and avidin monolayers can help to quantitate the changes in %R expected from an in situ SPR imaging experiment. Figure 31 plots the SPR reflectivity curves and differential reflectivity curves for these two monolayers obtained from an in situ cell utilizing an SF10 coupling prism. As shown in the figure, the SPR minima have shifted to higher angles as compared to the ex situ data, and the SPR reflectivity curves have broadened, due to the index of refraction of the monolayers being closer to that of aqueous solution than air. This broadening leads to a smaller differential reflectivity for a given change in thickness than that observed ex situ. However, the qualitative results are the same: if an SPR imaging experiment is performed at a fixed angle just below the SPR minimum, then an increase in the %R is observed as avidin adsorbs to the surface.

Figure 32 plots the line profiles from a series of in situ SPR imaging

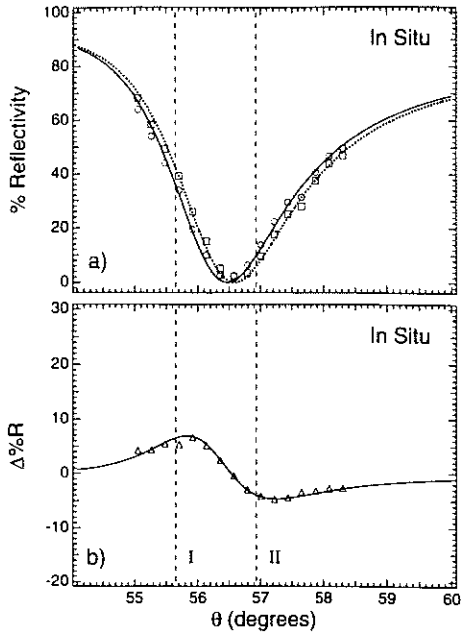

FIG. 31. SPR reflectivity and differential reflectivity curves for a PL monolayer and an avidin monolayer measured in situ. (a) The circles and the solid line show the experimental and theoretical SPR curves for a PL monolayer and the squares and dotted line show the same for an avidin monolayer. Notice that when measured in situ the SPR reflectivity curves are shifted to higher angles and are considerably broadened compared to the ex situ SPR curves shown in Fig. 28a for the same monolayers. (b) The differential reflectivity resulting from the SPR curves in (a); notice here that the differential reflectivities are much less than those seen in Fig. 28b. The dashed lines labeled I and II correspond to the two angles at which the calculated differential reflectivity vs. thickness is considered in Sec. IV.C.3. (From Ref. 129.)

measurements on MUA-PL surfaces identical to those used in the ex situ experiments. Notice that the two areas on the MUA-PL surface show a smaller difference in %R in this in situ experiment than in the corresponding ex situ experiment (Fig. 30), as predicted from the scanning SPR curves in Fig. 31. As in the ex situ measurements, exposure of this surface to an avidin solution results in the strong adsorption of the protein avidin onto the MUA monolayer portions of the surface (dashed line). Using the

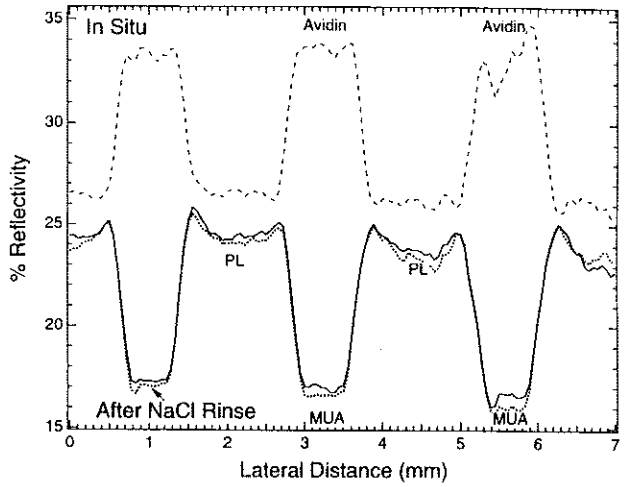

FIG. 32. Line profiles measured in situ for avidin adsorption onto a patterned MUA-PL surface and the subsequent removal of avidin by high electrolyte concentration. The solid line is the %R from a MUA-PL surface imaged in buffer and the dashed line is taken after exposure of the sample to a pH 8.5 avidin solution and rinsing with buffer. The dotted line is the %R measured in the buffer after exposure of the sample to 2 M NaCl (pH 8.5). The dotted line shows that a high concentration of electrolyte will remove all of the avidin from a MUA-PL surface, as expected for electrostatically bound avidin. (From Ref. 129.)

in situ measurements, the avidin adsorption is found to reach a constant level in about 5 minutes; this level of adsorption does not change when the avidin solution is replaced with pH 8 buffer.

Also shown in Fig. 32 is the line profile of the photopatterned SPR image after rinsing with a 2 M NaCl solution (dotted line). The line profile shows that the avidin monolayer has been completely removed upon exposure to a solution with high electrolyte concentration due to the screening of the PL and MUA charges. This observation agrees with our previous assertion that the avidin is adsorbed electrostatically to the MUA monolayer. The rate of desorption of the avidin and the residual amount of the protein on the surface varied with the salt concentration; complete desorption of the monolayer occurred within 20 minutes for all NaCl solutions above 1.0 M.

Interestingly, it is shown in the figure that the electrostatically adsorbed PL layer on the patterned sample does not desorb upon exposure to

the high-salt solution. However, if an electrostatically adsorbed PL monolayer is exposed to a high-salt solution directly after deposition, it will completely desorb as expected. It has been observed that if the PL/MUA bilayer is heated at 100°C for one hour before exposure to a 2 M NaCl solution, little or no PL desorption is detected. We hypothesize that this irreversible binding of the PL/MUA bilayer is due to hydrogen bond formation caused by dehydration and/or conformational changes which occur during heating. In the process of making the patterned MUA-PL samples (shown in Fig. 29) the PL/MUA bilayers were heated, and for this reason there was no loss of PL during the 2 M NaCl rinse shown in Fig. 32.

Further in situ SPR imaging experiments were performed in order to examine the effect of solution pH upon avidin adsorption to the MUA monolayer. As the pH is lowered, the carboxylic acid groups of the MUA monolayer should become protonated and the electrostatically adsorbed avidin molecules should desorb. The %R measured for an avidin mono-

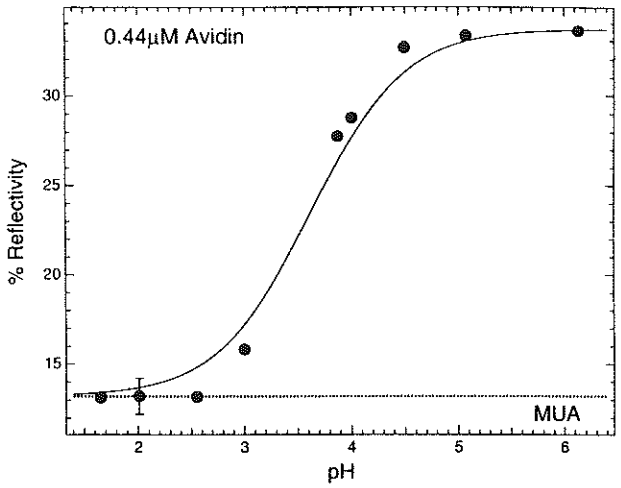

FIG. 33. The % reflectivity measured from a MUA surface in equilibrium with a 0.44 μM avidin solution as a function of solution pH. At a pH below 2.5 no avidin adsorbs to MUA. This can be seen by the overlap of the circles below pH 2.5 with the dotted line, where the dotted line shows the %R from MUA before exposure to avidin. At a pH greater than 4.5 the amount of avidin adsorption plateaus at a %R which corresponds to a full monolayer of avidin. This titration curve was fit to a Langmuir adsorption isotherm for $K_{ads} = 550$ (solid line). (From Ref. 129.)

layer adsorbed to a MUA SAM from a 0.44 μM solution is shown as a function of pH in Fig. 33; the data in this figure were obtained from a series of SPR imaging experiments of a MUA-PL surface. Above a pH of 4.5, a full avidin monolayer is adsorbed onto the MUA monolayer. However, below this pH only partial avidin monolayers are observed, and by pH 2.5 the avidin is completely removed from the surface. Further experiments (not shown) also indicate that avidin will completely desorb in a pH 13 solution. Since this pH is significantly above the pI of avidin, this observation also supports the assertion that avidin is electrostatically adsorbed to the MUA SAM. The pH at which 50% of an avidin monolayer is adsorbed to the MUA surface, as observed in Fig. 33, is significantly less than the measured pK_a for a MUA monolayer. This difference results from the fact that both the pK_a for the MUA surface and the ion pairing constant between avidin and the MUA monolayer are important in determining the surface coverage of electrostatically adsorbed avidin [129].

2. *Molecular Weight Dependence of Poly-L-*lysine Adsorption

Another factor that affects the electrostatic adsorption of polypeptides onto surfaces is the number of monomers in the polypeptide. In a second set of in situ SPR imaging experiments, this effect is examined by measuring the amount of PL adsorbed to MUA as a function of PL molecular weight. We have previously observed in ex situ measurements that PL molecules with an average of 67 lysine residues will form a full monolayer on a MUA surface when deposited from a pH 8.5 solution, but that lysine monomers will not adsorb at this pH [6]. Figure 34 shows the results of in situ SPR imaging experiments in which the amount of PL adsorbed onto a MUA monolayer was determined for a series of solutions with an average PL length that varied from 1 to 270 lysine residues. In these experiments, a constant lysine residue concentration of 0.7 mM was maintained in each solution. Each point in Fig. 34 was obtained by measuring the amount of PL adsorbed to the MUA portions of a gold thin film that was photopatterned with areas of MUA and 11 mercaptoundecanol (MUD). A striped MUA-MUD surface was used in these experiments since PL does not adsorb to a MUD SAM, and therefore the percent reflectivity of the MUD surface could be used as an internal standard. With these MUA-MUD surfaces, we were able to monitor the very small changes in the percent reflectivity observed for the partial monolayers formed on the MUA monolayer from low molecular weight PL. The MUA-MUD surface was regenerated in between exposures to the various PL solutions by rinsing with an acidic (pH

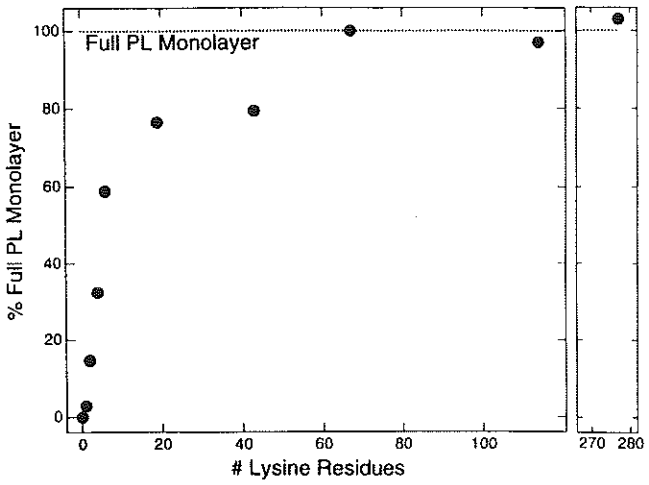

FIG. 34. The % of a full PL monolayer electrostatically adsorbed onto MUA as a function of the molecular weight measured in pH 8.5 solutions each with a constant lysine residue concentration of 0.7 mM. Percent reflectivities were obtained from a surface patterned with stripes of MUA and mercaptoundecanol (MUD). The percentage of a full PL monolayer was obtained by normalizing the difference in %R seen for each length PL on MUA to the maximum PL coverage. No adsorption is seen for L-lysine but the percent of adsorption increases rapidly with polymer chain length until a full monolayer of PL is adsorbed for chain lengths longer than 67 monomer units. (From Ref. 129.)

2) buffer. The percentage of a full monolayer (shown in Fig. 34) was obtained by normalizing the %R measured for each length PL on MUA to the maximum PL coverage. The amount of adsorbed PL increases quickly from no observable adsorption for lysine monomers to 60% of a monolayer for PL with 6 residues and then levels off until a plateau is reached at full monolayer coverages for chain lengths above 67 lysine residues. Since the lysine residue concentration is held constant during these experiments, the increased PL adsorption with chain length is due solely to an increased affinity between the longer PL molecules and the MUA surface. It was also determined that monolayers formed from PL solutions with average chain lengths greater than 19 residues showed no desorption when rinsed with a pH 8.5 buffer solution, but some loss of PL was observed for the shorter

PL chains upon rinsing. This indicates that, in addition to the adsorption coefficient, the adsorption kinetics are also affected by the polypeptide molecular weight.

3. *Multiple Oligonucleotide Hybridizations Onto Immobilized DNA*

In a final example, in situ SPR imaging has been used to detect the attachment of DNA oligonucleotide probes onto chemically modified gold surfaces and to characterize the subsequent in situ hybridization of oligonucleotide targets to these probes. As seen previously, SPR is sensitive to the thickness and index of refraction of an adsorbed layer. However, if the surface coverage of a particular analyte is low, it may be necessary to use some type of amplification strategy to improve the SPR response. In this section, an in situ chemical amplification strategy based on multiple DNA hybridizations is demonstrated as a means of improving the detection limit of DNA hybridization adsorption by SPR methods [169].

In this experiment, a DNA oligonucleotide containing 30 bases which is modified at the 5′ end with an amine group has been attached to a gold surface coated with MUA and electrostatically bound PL using the bifunctional linker 1,4-phenylene diisothiocyanate (PDITC) [170]. DNA which is covalently bound to the surface is referred to as "Probe" DNA in the inset of Fig. 35. Once the probe is bound to the surface, it is possible to hybridize a complementary (target) piece of DNA to it, shown as target A in the inset of Fig. 35. Target A is designed so that only half of its 30-base sequence is involved in hybridization to the surface probe and the remaining free bases can be used to hybridize a layer of target B to the surface. Target B can then hybridize a third strand of target DNA to the surface; in particular, its sequence is such that it will hybridize a second layer of target A. By sequentially exposing the surface to solutions of first target A and then target B, it is possible to perform multiple hybridizations to a single strand of probe DNA using only two different target oligonucleotides. Figure 35 shows the plot profiles from an in situ SPR imaging experiment where multiple hybridizations are used to amplify the SPR signal produced by the initial covalently bound probe DNA. In this experiment two spots containing amine-modified DNA with different sequences were created on a PDITC-modified gold surface and imaged in situ. The curve labeled "Probes" in Fig. 35 is a line profile taken through these two spots. A solution containing the complement to one of these DNA probes (target A) was injected into the in situ cell. It can be seen from line A1 in the figure that

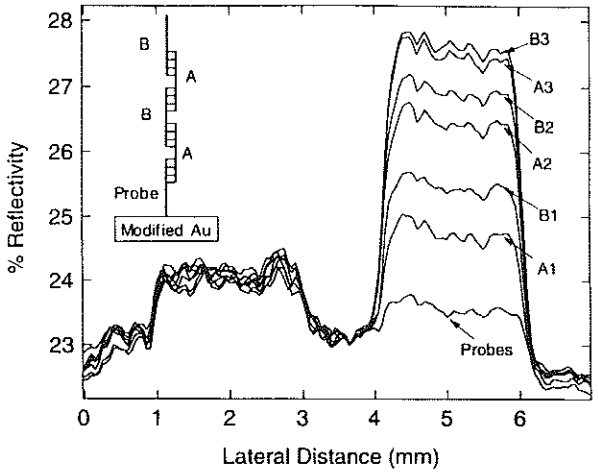

FIG. 35. Line profiles showing the amplification of the SPR response from DNA hybridization at a modified gold surface. The inset shows the strategy used to amplify the SPR response by hybridizing two different DNA oligonucleotides (A and B) to a single probe DNA molecule attached to the surface. The SPR line profile from a surface with two different DNA oligonucleotide probes immobilized on it is labeled "Probes" in the figure. Line A1 shows the response after exposing the surface to the complement to one of the DNA molecules. All of the bases in oligonucleotide A are not involved in hybridization to the probe and the free bases are able to hybridize to oligonucleotide B (line B1). A second exposure of the surface to oligonucleotide A results in further hybridization shown as line A2. More hybridization results from subsequent exposures to oligonucleotides B and A. (From Ref. 170.)

this complement adsorbs only to one of the spots, which clearly demonstrates the specificity of this surface hybridization. Then the sample was exposed to target B, and further adsorption to the spot was observed (line B1). This sequential hybridization will occur many times as shown by the increase in SPR response of each of the first five line profiles in Fig. 35. Notice that this increase is not linear, but levels out after five hybridization steps. There are two possible reasons for this behavior: the SPR response is not linear with increasing thickness, or hybridization efficiencies of each adsorption step are less than 100%.

The nonlinearity in the SPR response is quantified in Fig. 36, which

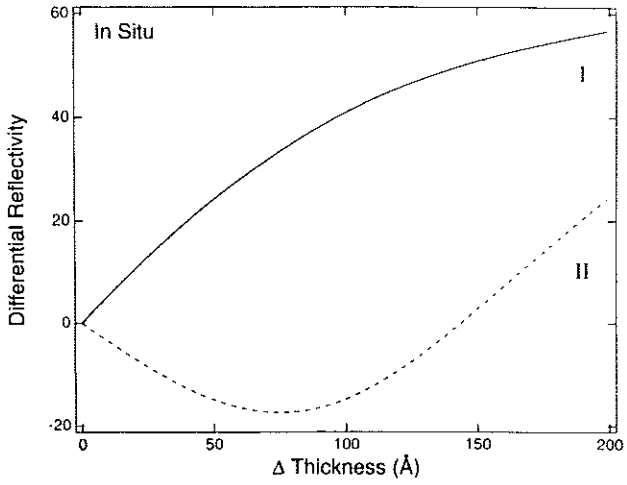

FIG. 36. Differential reflectivity vs. change in thickness of a thin film, with refractive index of 1.45, calculated in situ at two fixed angles shown as I and II in Fig. 31. The solid line is the differential reflectivity at angle I and shows a region of about 50 Å for which the differential reflectivity changes linearly with thickness before it starts to level out. The dashed line is the differential reflectivity at angle II and is an example of an angle where the differential reflectivity first decreases with increasing thickness.

plots the theoretical change in %R expected for an in situ SPR imaging experiment as a thin film with index of refraction of 1.45 adsorbs to the gold surface. For example, if an SPR imaging experiment is performed at the fixed angle labeled "I" in Fig. 31, the differential reflectivity would increase linearly over the first 50 Å and then slowly level out. In contrast, if an angle on the other side of the SPR minimum were chosen ("II" in Fig. 31), an initial decrease in the %R would be observed upon adsorption of the thin film. These two examples demonstrate that the change in differential reflectivity is highly dependent on the incident angle and so it cannot be assumed that the SPR response is linear with thickness. This problem can in principle be overcome by measuring the differential %R at multiple fixed angles. If the SPR imaging measurements are performed at multiple fixed angles such as those plotted in Figure 31, then changes in effective film thickness can be calculated more reliably during an adsorption experi-

ment, and the SPR imaging apparatus can be used to examine films over a wider range of thicknesses.

The magnitude of the increase in %R per hybridized layer shown in Fig. 35 certainly does drop off, but is this decrease due to the inherent nonlinearity in the SPR response or to a low hybridization efficiency? After the six hybridization steps were performed, the incident angle at which the images were taken was increased. A seventh hybridization step was subsequently performed and the SPR response increased by approximately 1 %R (data not shown). The fact that this increase is larger than that seen at the original angle for the sixth hybridization indicates that the continuously smaller changes in SPR signal must be at least partially due to the nonlinear increase in the differential reflectivity with added thickness. This experiment indicates that multiple DNA hybridizations can best be characterized by measuring the SPR imaging response at multiple fixed angles.

As these examples show, the use of SPR imaging experiments for differential adsorption measurements at patterned surfaces is a natural extension of the SPR scanning measurements. SPR imaging experiments have been used to investigate the adsorption of proteins, polypeptides, and oligonucleotides onto chemically modified gold surfaces. SPR imaging is well suited for these studies because (1) adsorption onto a patterned array of several chemically different surfaces can be observed simultaneously with this technique, (2) any sample-to-sample variations in both ex situ and in situ differential adsorption measurements can be eliminated by using these patterned surfaces, and (3) quantitative adsorption information can be readily extracted from the resulting SPR images and line profiles. In the next section, in situ SPR experiments are applied to an electrochemical environment in order to measure the electrostatic fields within self-assembled multilayer films on a gold electrode surface.

V. SPR ELECTRIC FIELD MEASUREMENTS

A. Introduction

In an electrochemical environment, the optical technique of SPR has been used to probe a variety of chemical and physical processes at metal surfaces. We have recently demonstrated that a novel extension of the surface plasmon resonance technique called electrochemically modulated surface plasmon resonance (EM-SPR) can be used to monitor electrostatic fields

inside organic monolayer and multilayer films at electrode surfaces [64]. The strength of the electrostatic fields within the interfacial region of a chemically modified electrode is a fundamental parameter that controls the reactivity and electrochemistry of any chemical species incorporated into the thin film [171–176]. To date, there have been a limited number of studies that have determined field strengths within monolayer films at electrode surfaces [177–182], and only a few measurements of the variations in the electric fields as a function of position in the ultrathin film have been reported [183–185]. In this section, we describe the EM-SPR technique and demonstrate how it can be used to determine the electric field strength and field profile within noncentrosymmetric self-assembled zirconium phosphonate (ZP) multilayer films at electrode surfaces.

B. EM-SPR Theory

The EM-SPR technique utilizes surface plasmons to measure the minute changes in the index of refraction of a noncentrosymmetric thin organic film that occur upon application of an external electrostatic field. The change in index of refraction (Δn) of a film upon application of an external electric field is referred to as the linear electro-optical effect [186]; this response requires a noncentrosymmetric material and is described by the electro-optic coefficient, r. The electro optic coefficient is a tensor quantity, and for a non-birefringent material the tensor element r_{33} has the general form of [96]:

$$r_{33} = \frac{2\Delta n_z}{n^3 \Delta E_z} \tag{3}$$

where n is the isotropic index of refraction of the material and Δn_z is the change in n in the z-direction created by a change in an applied field along the z-axis, ΔE_z. The value of r_{33} for ultrathin noncentrosymmetric ZP films of the molecules HAPA ([5-[4-[[4-[(6 hydroxyhexyl) sulfonyl]phenyl]azo]phenyl]pentoxy]phosphonic acid) and PY AZO ([1-[4-[4-[(*N*-(2-hydroxyethyl)-*N* methyl)amino]phenyl]azo](5-phosphonopentyl)] pyridinium bromide) (see Fig. 37a) has been determined from modulated SPR experiments on air-gap capacitors; these r_{33} measurements are described in more detail in Sec. V.D.

As in the scanning SPR measurements discussed in Sec. III, surface plasmons are created at a gold/electrolyte interface in an EM-SPR experiment by the prism coupling of a HeNe laser to a thin gold film at the SPR

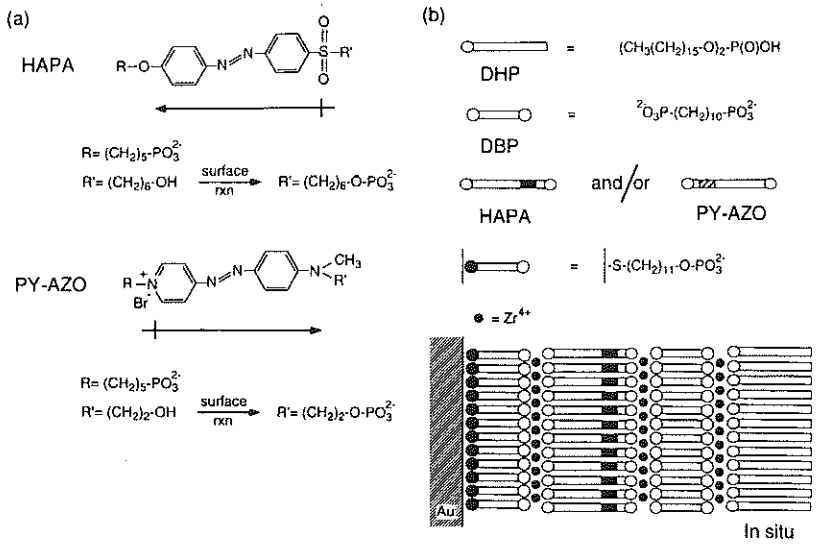

FIG. 37. (a) The structures and associated dipole moments (black arrows) for the nonlinear optical chromophores HAPA ([5 [4-[[4-[(6-hydroxyhexyl)sulfonyl]phenyl]azo]phenyl]pentoxy]phosphonic acid) and PYAZO ([1-[4-[4-[(*N*-(2-hydroxyethyl)-*N*methyl)amino]phenyl]azo](5-phosphonopentyl)]pyridinium bromide) used in these experiments to form noncentrosymmetric zirconium phosphonate (ZP) multilayer films on gold surfaces. (b) Schematic diagram for the construction of noncentrosymmetric mixed zirconium phosphonate multilayer films. The ZP films are created on vapor-deposited gold substrates that have been primed with a self-assembled monolayer of phosphorylated MUD. Exposure of the zirconated surface to solutions of the nonlinear optical compounds HAPA and/or PY-AZO following the procedure of Katz and co-workers led to noncentrosymmetric multilayer films. For electric field profile experiments, N DBP (1,10-decane diylbis(phosphonate)) layers where N = 0–8 are self-assembled onto the HAPA monolayer. The films were then capped with a self assembled monolayer of DHP (dihexadecyl phosphate), and characterized in an electrochemical environment with EM-SPR. (From Ref. 105.)

angle (θ_{sp}). This SPR angle depends upon the thickness and index of refraction of the dielectric medium in contact with the metal surface. The EM-SPR experiment measures shifts in θ_{sp} by the changes in reflectivity (Δ%R) that occur upon potential modulation ($\Delta\phi_m$) as a function of incident angle θ. These experimental EM-SPR "differential reflectivity" or "Δ%R" curves are modeled with complex Fresnel calculations in order to

relate the measured Δ%R to the change in the film's index of refraction Δn. From this Δn value, the change in electric field strength (ΔE) within the film due to potential modulation at a charged electrode can be determined by [96,187]:

$$\Delta E = \frac{2\Delta n}{n^3 r_{33}} \tag{4}$$

where n is the optical index of refraction of the film and r_{33} is the electro-optic coefficient for the noncentrosymmetric ZP film determined previously. Note that in Eq. (4) we have dropped the z subscripts on ΔE and Δn since the electric fields are always normal to the electrode surface (defined as the z-direction).

The linear electro-optical effect is a nonlinear optical mixing process similar to optical second harmonic generation (SHG) where one of the electric field components is at zero frequency [186]. The electro-optic coefficient r_{33} for the noncentrosymmetric ZP films can be related to the complex second-order surface nonlinear susceptibility $\chi_{zzz}^{(2)}(-\omega; \omega, 0)$ by [96,188–190]:

$$\chi_{zzz}^{(2)}(-\omega; \omega, 0) = -n^4 r_{33} \tag{5}$$

This surface nonlinear susceptibility has both a magnitude and a phase component associated with it. In Sec. V.E.3 the phase of the electro optical signal is used to determine the relative orientation of different nonlinear optical chromophores in mixed ZP multilayer films.

C. Noncentrosymmetric Zirconium Phosphonate Multilayer Films

As discussed in Sec. V.B, the linear electro-optical effect is nonzero only for noncentrosymmetric thin films. This requirement can be satisfied by the creation of self-assembled multilayer films based on the zirconium phosphonate (ZP) ligand chemistry first reported by Mallouk and coworkers for centrosymmetric films [159,160] and subsequently modified by Katz et al. to create noncentrosymmetric multilayers [162,191,192]. For the EM-SPR experiments described here, ultrathin (<50 nm) noncentrosymmetric organic films were formed on gold substrates by the sequential deposition of self-assembled zirconium phosphonate monolayers of the molecules HAPA or PY-AZO (see Fig. 37a). The HAPA molecule contains an azobenzene nonlinear optical (NLO) chromophore with sulfonyl electron-accepting and phenyl ether electron-do-

nating groups, and is terminated with a phosphonic acid on one end and an alcohol functional group on the other. The PY-AZO molecule consists of a pyridinium electron-accepting group and an amino electron-donating group separated by an azodye Π-conjugated ring system. HAPA and PY-AZO were synthesized because of their large molecular hyperpolarizabilities and dipole moments. Note that the dipole moment of PY-AZO points in the opposite direction of the HAPA molecule; i.e., in PY AZO, the dipole moment points away from the phosphonate group as compared to the dipole moment in HAPA, which points towards the phosphonate end of the molecule.

Noncentrosymmetric films of HAPA or PY-AZO were formed by the method outlined by Katz et al. (see Fig. 37b), in which the NLO chromophore adsorbs as a self-assembled monolayer on a Zr^{4+} ion–coated primer layer composed of phosphorylated MUD (11 mercaptoundecanol) via the phosphonic acid group, and then the terminal alcohol groups on the other end of the molecules are converted to phosphates which can bind a new monolayer of Zr^{4+} ions for the adsorption of additional monolayers [153,162]. The in situ electric field profile measurements in Sec. V.E.2 employed mixed noncentrosymmetric ZP films that contained the centrosymmetric molecule DBP (1,10 decanediylbis(phosphonate)) and were terminated with a self-assembled monolayer of DHP (dihexadecyl phosphate). This DHP capping monolayer produced very hydrophobic gold electrode surfaces that helped decrease electrolyte penetration into the film. These films were all characterized with a combination of scanning SPR and PM-FTIRRAS as detailed in Sec. III.D prior to performing modulated SPR measurements.

D. Modulated SPR Measurements on Air-Gap Capacitors

The determination of the linear electro-optic coefficient r_{33} for a ZP/HAPA monolayer film was accomplished by the use of modulated SPR measurements on air-gap capacitors. This method has been used previously for the determination of the electro-optic coefficients of ultrathin Langmuir-Blodgett NLO organic films and micron thick NLO poled-polymer films [64,91–94,96,98–104]. In these experiments, the ultrathin NLO organic film is deposited onto a thin (47 nm) gold film that serves as one electrode of an air-gap capacitor as shown in Fig. 38. An external AC voltage (on the order of 10–50 V with a frequency of 1–10 kHz) is applied to the capacitor in order to create an oscillating electrostatic field on the order of 10^4 V/cm that modulates the index of refraction of the ultrathin NLO organic film via

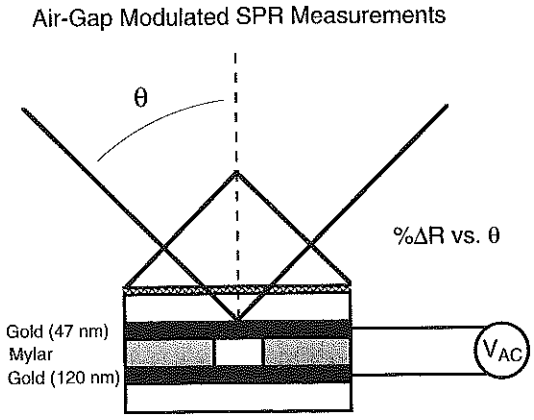

FIG. 38. The modulated surface plasmon resonance apparatus used for the determination of the electro-optical response of noncentrosymmetric ZP films. This apparatus measures the reflectivity (%R) and differential reflectivity (Δ%R) of p-polarized light at 632.8 nm (HeNe laser) from the BK7/Au/ZP film/air interface as a function of incident angle, θ. The samples for these experiments consist of a thin Mylar dielectric film which is pressed between the ZP modified gold samples and a second gold electrode. A small square is cut out of the Mylar so the surface plasmon wave is evanescent in air upon excitation. Electrical contact is made to the two gold surfaces, and a sinusoidal waveform is applied across the gap.

the electro-optical effect. This change in the index of refraction results in a shift of the SPR angle that can be observed by detecting the modulated change in reflectivity as a function of incident angle, θ.

Figure 39 plots the modulated change in reflectivity (Δ%R) observed for a single ZP/HAPA monolayer film as a function of incident angle near the surface plasmon angle (θ_{sp}). This signal was obtained by the application of a sinusoidal voltage $\Delta V = 30$ V at a frequency of 10 kHz across the air-gap capacitor. The thickness of the air-gap in the capacitor in this experiment was determined from capacitance measurements to be 15 μm, and a static or zero frequency dielectric constant ε of six was assumed for the ZP/HAPA monolayer films. (This value was chosen to match the experimentally determined dielectric constant for similar NLO azodye multilayer ZP films reported by Katz et al. [193]). The conditions of this experiment corresponded to an electric field strength $\Delta E = \Delta V/\varepsilon d$ of $3.3 \times$

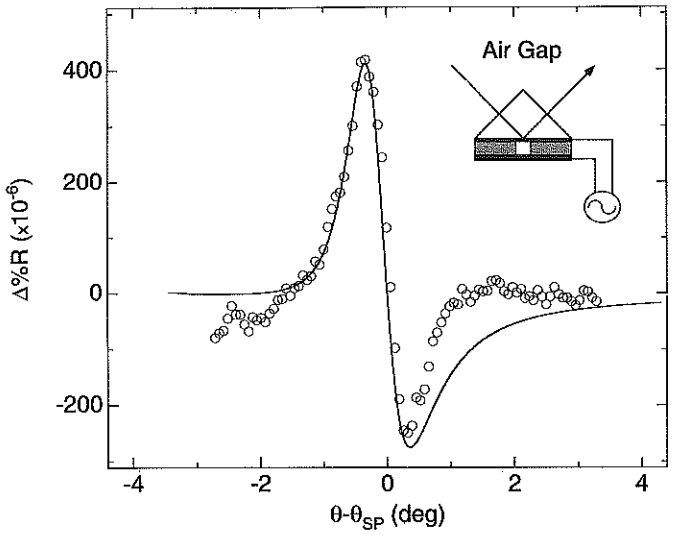

FIG. 39. Differential reflectivity (Δ%R) obtained by modulated surface plasmon resonance measurements in air for a ZP film consisting of a monolayer ZP/HAPA film formed onto a primer layer on a thin gold film. This signal which is attributed to a modulation in the dielectric constants of the HAPA monolayer through the linear electro-optical effect is obtained from application of a sinusoidal waveform (±15 V, 10 kHz) applied across the air gap (15 μm). The differential reflectivity caused by this modulation is recorded as a function of the incident angle, θ. The solid line in the figure is a complex Fresnel fit to the data obtained by varying the real component of the dielectric constant of the HAPA layer. (From Ref. 64.)

10^3 V/cm within the ZP/HAPA monolayer film. The change in reflectivity at 10 kHz was obtained by lock-in amplifier detection of the photodiode current (see Sec. III.C) and has the functional form of the derivative of the standard surface plasmon reflectivity curve. The magnitude of the differential reflectivity (Δ%R) increased linearly with the applied AC voltage for the HAPA sample as expected and was constant over the frequency range of 1–10 kHz. In addition, no signal was observed in the absence of the ZP/HAPA monolayer.

These experimental modulated SPR differential reflectivity curves can be modeled with complex Fresnel calculations in order to relate the measured Δ%R to the change in the film's index of refraction Δn. An exam-

ple of how Fresnel calculations can be used to relate Δ%R and Δn is depicted in Fig. 40. Figure 40a plots two surface plasmon theory curves for two thin films that differ in index of refraction. The difference between these two curves produces the differential reflectivity curve shown in Fig. 40b. This theoretical Δ%R curve is used to fit the experimental air-gap SPR data and results in the determination of Δn for a given ΔE. The solid line in Fig. 39 is a five-phase Fresnel calculation in which the real part of the index of refraction for the HAPA monolayer is varied by $\Delta n = 8.0 \times 10^{-6}$. (Only the real component of the refractive index was considered because the HAPA monolayer does not absorb at the wavelength employed in this ex-

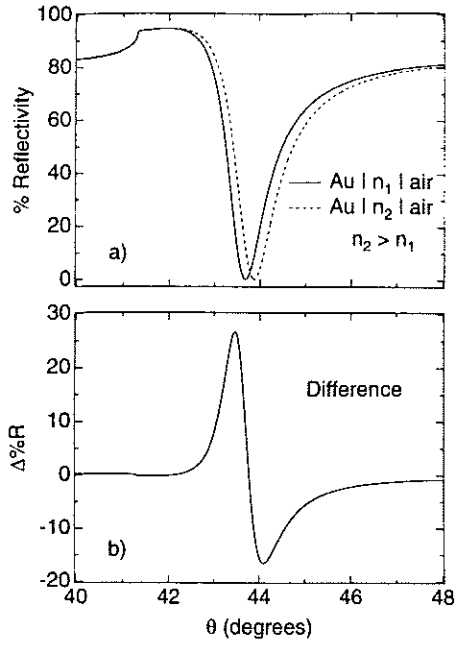

FIG. 40. Method for modeling the measured air-gap modulated SPR differential reflectivity curves. (a) Two surface plasmon curves generated from Fresnel calculations which differ in the film's index of refraction. (b) The differential reflectivity curve produced from the difference between the two curves in (a). This theoretical Δ%R curve is used to fit the experimental modulated SPR data and results in the determination of Δn for a given ΔE. (From Ref. 105.)

periment.) A similar change in the SPR reflectivity can be obtained by a change in the thickness of the film (Δd) with applied voltage but we assume that all changes are due to index of refraction effects via the electro-optic coefficient. Using Eq. (3), a change in Δn of 8.0×10^{-6} corresponds to an electro optic coefficient r_{33} of 11 pm/V at 632.8 nm. This r_{33} is an off-resonance value since the monolayer film does not absorb light at this wavelength. From the value of r_{33}, the surface nonlinear susceptibility $\chi_{zzz}^{(2)}$ $(-\omega; \omega,0)$ for the ZP film is calculated from Eq. (5) to be 41 pm/V (9.7×10^{-8} esu). Using this $\chi_{zzz}^{(2)}$, the HAPA molecular hyperpolarizability $\mathbf{b}_{zzz}$ is estimated to be 9.3×10^{-29} esu at 632.8 nm, assuming a chromophore tilt angle of 27° as obtained from second harmonic generation (SHG) experiments and a number density for the HAPA molecules in the ZP film of 10^{21} molecules/cm^3 [194]. The magnitude of the electro-optic coefficient in these ZP films is less than that for $LiNbO_3$ (31 pm/V), but is within the range of the values observed in NLO poled polymer films (1–55 pm/V) [96,188–190,195–198]. Moreover, the noncentrosymmetric character of the HAPA monolayer did not decrease with time, as is often the case for the polymer systems. Similar air-gap capacitor modulated SPR experiments were performed on a monolayer PY-AZO film, and an electro-optic coefficient of –8 pm/V at 632.8 nm was obtained. The negative sign indicates that the relative electro-optical response of the PY-AZO monolayer is opposite to that observed for the HAPA monolayer, as expected from the difference in the direction of the dipole moment for the two chromophores [106].

E. EM-SPR Measurements on Multilayer Films at Electrode Surfaces

1. Electric Field Measurements

The SPR modulation experiments used with the air-gap capacitors can also be applied to in situ electrochemical environments to monitor the electrostatic fields within ultrathin organic films via the electro-optical effect. In this electrochemically modulated surface plasmon resonance (EM-SPR) experiment, the electrochemical potential of the gold electrode is modulated sinusoidally with a magnitude $\Delta\phi_m$. The EM-SPR experiment measures the change in reflectivity that occurs due to this potential modulation as a function of incident angle θ. As in the air-gap SPR experiments, these experimental EM-SPR differential reflectivity (Δ%R) curves can be modeled with complex Fresnel calculations in order to determine the change in the film's index of refraction (Δn) for a given $\Delta\phi_m$. Using this Δn value and

the value of r_{33} obtained from the SPR air-gap experiments, the change in electric field strength (ΔE) within the film due to the potential modulation can be determined from Eq. (4).

A schematic diagram of the electrochemical cell used in the EM-SPR experiments is shown in the inset of Fig. 41. This cell consisted of a simple teflon body pressed against the modified gold electrode with an o-ring seal. A three-electrode potentiostat with the thin gold film as the working electrode was used to apply the potential modulation. A cyclic voltammogram (CV) of a gold electrode coated with a mixed HAPA/DBP multilayer film of thickness 13 ± 1 nm (as determined from in situ SPR scanning measurements) is shown in Fig. 41. The cyclic voltammetry ex-

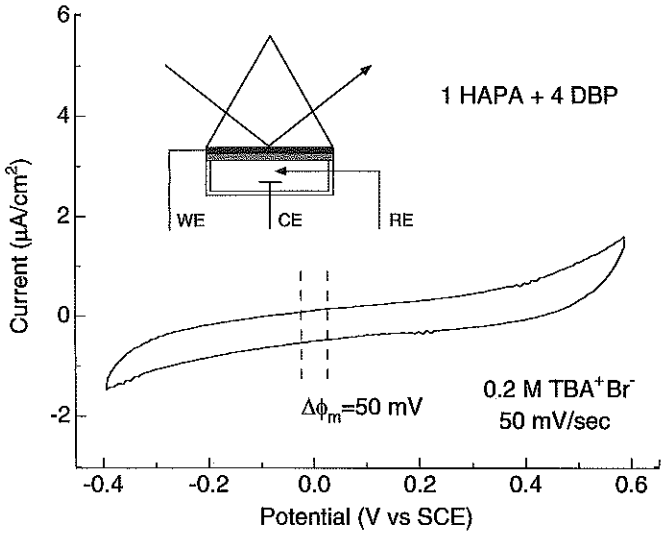

FIG. 41. Cyclic voltammogram for a 13 ± 1 nm thick ZP multilayer film that consisted of a phosphorylated MUD primer layer, one HAPA monolayer, four DBP monolayers, and one DHP capping monolayer on a vapor-deposited gold substrate. This sample is referred to as the "1 HAPA + 4 DBP" ZP film. A three-electrode assembly was formed with the ZP coated Au film as the working electrode, a saturated calomel reference electrode, and a platinum counter electrode. The CV was obtained in the region from –0.4 to 0.6 V vs. SCE in 0.2 M tetrabutylammonium bromide at a scan rate of 50 mV/sec. For EM-SPR, the electrode potential was fixed to 0.0 V vs. SCE and a small sinusoidal modulation ($\Delta\phi_m$ = 50–760 mV, at 1 kHz) was applied to the cell. (From Ref. 105.)

hibited no faradaic processes over a wide potential range from –0.4 to 0.6 V vs. SCE. For the EM-SPR experiments, the electrode potential was set to 0.0 V vs. SCE, and a sinusoidal waveform $\Delta\phi_m$ of 50–760 mV was applied at a frequency of 1 kHz. No changes in the measured EM-SPR response were observed for modulation frequencies from 0.2 to 1.5 kHz.

Typical in situ EM-SPR differential reflectivity curves obtained from a potential modulation of 50 mV are plotted in Fig. 42. Two Δ%R curves are shown in the figure: the open squares are data from a 6.7 nm ZP/HAPA

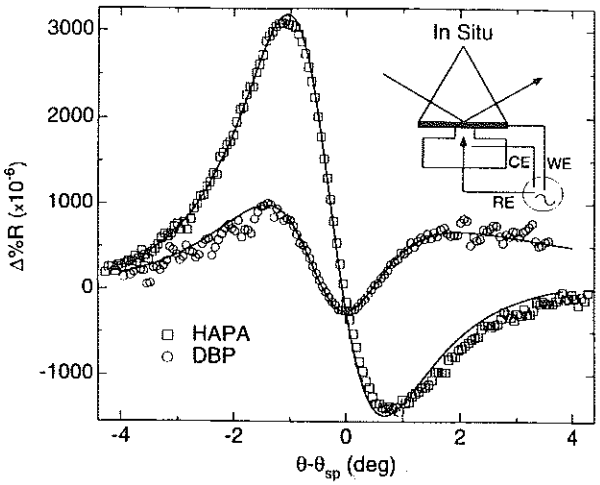

FIG. 42. Differential reflectivity (Δ%R) obtained by EM-SPR measurements made in situ. The sample for this experiment shown in the inset of the figure consists of a teflon cell which is pressed against the ZP modified gold sample. A three-electrode assembly is made with the ZP modified gold sample as the working electrode. A potentiostat controlled the applied potential relative to SCE. A small sinusoidal waveform (50 mV, 1 kHz) was then applied to the cell at a potential where no electrochemistry took place. The open circles are obtained for a ZP film consisting of two monolayers of DBP, and one monolayer of DHP formed onto a prime layer on a thin gold film. This signal results from a modulation in the gold dielectric constants. The open squares are obtained for a ZP film consisting of one monolayer of HAPA, and one monolayer of DHP formed onto a primer layer on a thin gold film. The solid lines for both sets of data are complex Fresnel fits obtained by varying the real component of the dielectric constant of the HAPA layer and the gold. (From Ref. 64.)

film consisting of a single HAPA monolayer film formed on a phosphorylated MUD primer monolayer and capped with a DHP monolayer (see Fig. 37b), and the open circles are the data obtained for a centrosymmetric ZP/DBP multilayer consisting of a primer monolayer of phosphorylated MUD, followed by two layers of DBP and one capping layer of DHP. The modulation in the SPR signal from the centrosymmetric film results solely from the electro-optical contributions of the gold electrode substrate. This effect was not observed in the air-gap experiment to within the signal-to-noise ratio of the experiment, but changes in the optical constants of metal electrode surfaces have been observed previously in electroreflectance measurements [17,68]. The solid line that fits these data is a seven-phase Fresnel calculation which assumes that the real part of the index of refraction of the first 0.05 nm of the gold electrode surface changes upon modulation of the electrode potential by an amount $\Delta n = -1.6 \times 10^{-3}$. The thickness of this layer is taken as 0.05 nm in order to approximate the Thomas-Fermi screening depth of the metal [17]. Increasing this thickness reduced the size of Δn, but had no effect on the shape of the calculated fit. Note that for these data, the minimum in $\Delta\%R$ occurs at the surface plasmon angle θ_{sp}.

In contrast, the larger differential reflectivity curve in Fig. 42 obtained from the *noncentrosymmetric* HAPA film exhibits a minimum and a maximum in $\Delta\%R$ above and below θ_{sp}, respectively, as observed previously in the HAPA air-gap capacitor experiments. The solid line that fits the data is a seven-phase Fresnel fit taking both the modulation of the index of refraction of the HAPA monolayer and the modulation of the index of refraction of the gold surface into account. This theoretical fit yields a value for the change in index of refraction for the HAPA monolayer of $\Delta n = 3.3 \times 10^{-5}$.

Using the value of r_{33} determined for a HAPA monolayer in Sec. V.D, the experimentally determined Δn for the ZP/HAPA film can be related to the change in electric field strength (ΔE) within the multilayer films at the electrode surface. The value for Δn of the HAPA monolayer film is a factor of four greater than that measured in the air-gap experiment, and therefore corresponds to a change in electric field strength during potential modulation of 1.4×10^4 V/cm for $\Delta\phi_m = 50$ mV (2.8×10^5 V/cm for $\Delta\phi_m = 1$ V) within the ultrathin organic film.

A second set of EM-SPR experiments is shown in Fig. 43, which plots the differential reflectivity curves observed from the "1 HAPA + 4 DBP" mixed multilayer for a series of different modulation potentials. The

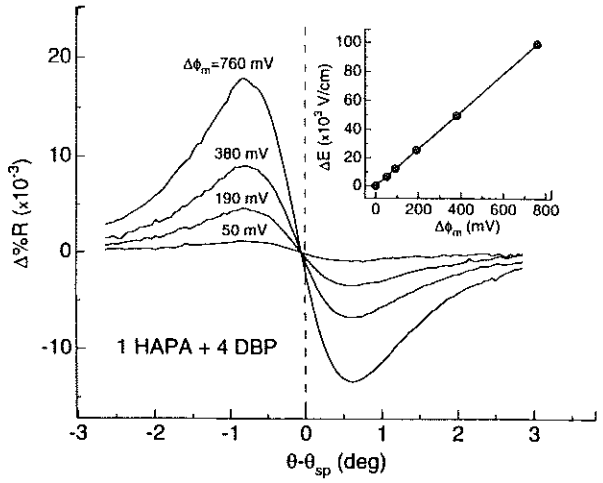

FIG. 43. Differential reflectivity (Δ%R) obtained by EM-SPR measurements in 0.2 M tetrabutylammonium bromide for the 1 HAPA + 4 DBP ZP film. The curves are the overlay of increasing electrode modulation potentials ($\Delta\phi_m$) of 50, 190, 380, 760 mV about 0.0 V vs. SCE, at 1 kHz, respectively. The differential reflectivities (Δ%R) measured in situ are converted to a change in electric field strength (ΔE) within the self-assembled multilayer film by comparison to air-gap electro-optical experiments. The change in the electric field strengths within the multilayer ZP film shown in the inset graph are surprisingly linear with the applied modulation potential in the experimentally measured electrochemical potential window from –0.4 to 0.6 V vs. SCE. (From Ref. 105.)

shape of the Δ%R curves does not change with increasing modulation voltage and is similar to the HAPA monolayer film. The Fresnel calculations predict a zero-crossing point of θ-θ_{sp} = –0.06° for all of the Δ%R curves; this prediction agrees with the experimental data in the figure. From the Fresnel fits of the data, values for Δn are obtained and range from Δn = 1.6 × 10^{-5} for $\Delta\phi_m$ = 50 mV to Δn = 2.4 × 10^{-4} for $\Delta\phi_m$ = 760 mV. The ΔE values obtained from these Δn values by Eq. (4) are plotted as a function of $\Delta\phi_m$ in the inset graph of Fig. 43. The change in field strength is found to be surprisingly linear for applied modulation potentials from 0 to 760 mV and corresponds to a ΔE of 6.5 × 10^3 V/cm for a $\Delta\phi_m$ of 50 mV (1.3 × 10^5 V/cm per volt modulation). These values for ΔE within the 13 ± 1 nm mul-

tilayer ZP film are consistent with the field strengths determined by Pope and Buttry inside a monolayer film at a silver electrode from fluorescent shift measurements [179,180].

We have also recently examined the EM-SPR response of ZP films incorporating the noncentrosymmetric molecule PY-AZO (pictured in Fig. 37a) [106]. The EM-SPR differential reflectivity (Δ%R) signal observed from a chemically modified gold sample that consisted of phosphorylated MUD, three PY-AZO monolayers, and one DHP monolayer is shown in Fig. 44. The series of curves labeled a–e are the overlay of increasing modulation potentials ($\Delta\phi_m$ = 50–200 mV). As with the ZP/HAPA films, the electro-optical signals were linear with the applied modulation potential. The shape of the PY-AZO EM-SPR differential reflectivity curves was constant with increasing modulation voltage, and the minimum and maximum in Δ%R occur to the left and right of θ_{sp}, respectively. This is the reverse of that measured for the ZP/HAPA samples and is due to the opposite

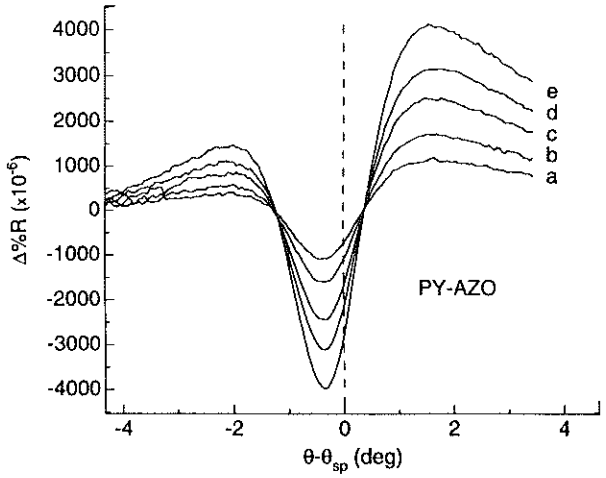

FIG. 44. Differential reflectivity (Δ%R) obtained by electrochemically modulated surface plasmon resonance measurements in 0.2 M tetrabutylammonium bromide for a three-layer ZP/PY-AZO sample. The curves labeled a–e are the overlay of increasing electrode modulation potentials ($\Delta\phi_m$) of 50, 80, 120, 160, 200 mV about 0.0 V vs. SCE, at 1 kHz, respectively. The measured differential reflectivity is a result of the electro-optical effect. (From Ref. 106.)

sign of r_{33} for these two films. Although the Δ%R curves indicate that the phase of $\chi^{(2)}(-\omega, \omega, 0)$ for the PY-AZO films is opposite that of HAPA films, the shape of the differential reflectivity waveforms is not exactly inverted due to the contributions from the gold substrate. Note also that the curves in Fig. 44 contain two zero-crossing points, one on each side of θ_{sp}. The Δ%R curves for ZP/HAPA films contain only one zero crossing point of the left of θ_{sp}; this difference is due to the substrate contributions to the differential reflectivity.

The EM-SPR response from the ZP/PY-AZO multilayer films was again modeled with theoretical Fresnel calculations. Figure 45 plots a seven phase Fresnel calculation of the differential reflectivity curve for a ZP/PY-AZO monolayer film where the underlying surface gold layer is taken into account. Note that the shape of the theoretical curves very accurately fit the experimental data. From these calculations, the change in index of refraction for the PY-AZO monolayer was determined to be Δn =

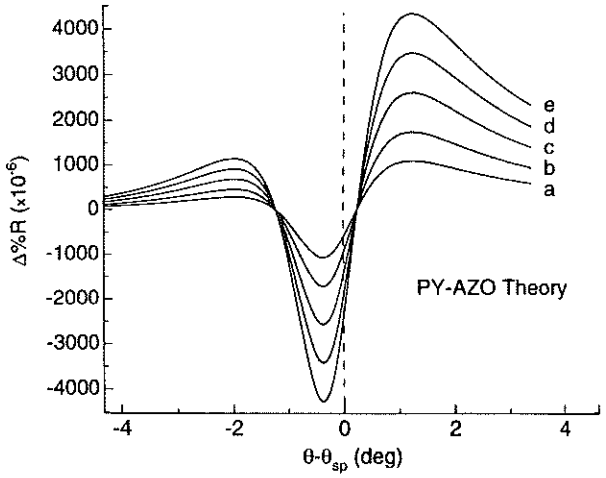

FIG. 45. Theoretical Fresnel differential reflectivity (Δ%R) calculations for a ZP/PY-AZO sample. The curves labeled a–e are the difference of two surface plasmon curves which differed by increasing values of $\Delta n_{Au} = (-1.4, -2.3, -3.4, -4.5, -5.6) \times 10^{-3}$, respectively, in the real component of the index of refraction of the surface gold layer (0.05 nm) and $\Delta n = (-1.4, -2.3, -3.4, -4.5, -5.6) \times 10^{-5}$, respectively, for the ZP/PY-AZO film. (From Ref. 106.)

-1.4×10^{-5} for $\Delta\phi_m = 50$ mV. This value of Δn is less than half that measured for a ZP/HAPA monolayer film. Air-gap electro-optical experiments indicate that the signal levels for PY-AZO and HAPA films should be approximately equivalent in magnitude (–8, 11 pm/V, respectively). The lower than expected Δn for the PY AZO sample implies that there is a decrease in the electrostatic fields inside the PY-AZO film as compared to the HAPA film due to more ion and solvent penetration into the multilayer. This result is reasonable given that, unlike HAPA, the PY-AZO species is charged and the film must contain additional counterions.

2. Electric Field Profile Measurements Inside Multilayers

In a series of experiments on mixed HAPA/DBP multilayers, EM-SPR measurements were used to map out the electric field profile within ultrathin films at electrode surfaces [105]. In these experiments, a single HAPA monolayer was used to probe the electric field at a specific point within the ZP film. A first set of EM-SPR experiments was performed on a series of five HAPA/DBP monolayers that consisted of a phosphorylated MUD primer monolayer, one HAPA monolayer, N DBP monolayers (where N varied from 0 to 8), and a DHP capping monolayer. In each of these films, the HAPA monolayer was the first ZP monolayer deposited onto the electrode surface. The mixed multilayer films were characterized prior to the EM-SPR experiments with PM-FTIRRAS and scanning in situ SPR measurements (see Sec. III.D.3). These measurements indicate that the thicknesses of the ZP films increase by 1.6 ± 0.2 nm per DBP monolayer (total film thicknesses from 6.7 to 20 nm for 0–8 DBP overlayers) with no observable changes in HAPA film structure and packing density. This DBP monolayer thickness is equivalent to that measured ex situ for multilayer DBP films in Sec. III.D.2. These results indicate that stable, reproducible mixed multilayers of HAPA and DBP are formed on the gold electrode surface. The change in electric field strength at the HAPA monolayer position for a $\Delta\phi_m$ of 50 mV was determined from EM-SPR differential reflectivity measurements on each of the films; the results of these experiments are plotted in Fig. 46. A decrease in ΔE of up to 65% is observed as the number of centrosymmetric DBP monolayers is increased.

This decrease in the measured EM-SPR signal is attributed to the increase in overall thickness (d) of the ZP film due to the formation of DBP overlayers and has the functional form of 1/d. A simple Helmholtz model of the electrochemical double layer also predicts that the electric field strength should decrease with film thickness as 1/d assuming a fixed static

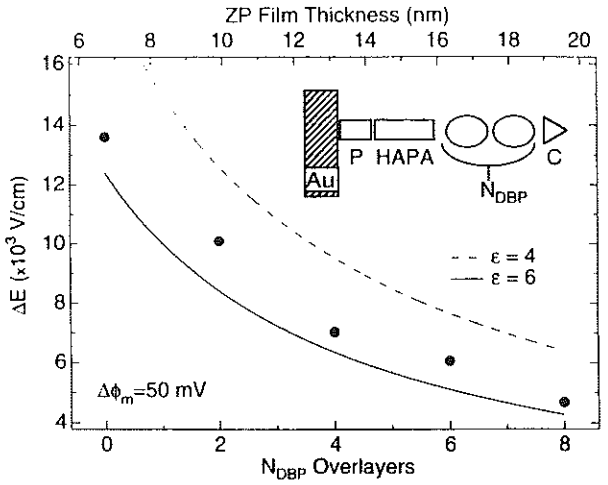

FIG. 46. Change in electric field strength (ΔE) within a noncentrosymmetric ZP/HAPA film for increasing numbers of DBP overlayers (N_{DBP} = 0–8). The ΔE values are determined via the EM-SPR differential reflectivity curves for a HAPA monolayer whose position was fixed in the film (see inset). The positions labeled P and C in the inset correspond to the phosphorylated MUD primer layer and the DHP capping monolayer, respectively. The solid and dashed lines are fits to the experimental data using a simple Helmholtz model. (From Ref. 105.)

dielectric constant ε [171]. For pure ZP films of DBP and HAPA-like chromophores, the static dielectric constants have been determined previously to be four and six, respectively [193,199]. The solid line in Fig. 46 is a theory curve generated from the Helmholtz model using the ZP film thicknesses determined from in situ and ex situ SPR measurements and a static dielectric constant of six. The dashed line in the figure is the same theory curve except using a value of 4 for ε. Although the experimentally determined ΔE values parallel the Helmholtz model using an ε of 6, the effective dielectric constant for these mixed ZP films should vary from 6 to 4 as more DBP overlayers are assembled.

Deviations from a simple Helmholtz picture for the measured ΔE values inside the ZP multilayers are even more apparent in a second set of experiments. In these measurements, a series of mixed HAPA/DBP films were prepared in which the total thickness was held constant and the posi-

tion of the HAPA monolayer was varied. These films consisted of a phosphorylated MUD prime layer, one HAPA monolayer, six DBP monolayers, and a DHP capping monolayer ("1 HAPA + 6 DBP" ZP films). As depicted in the inset of Fig. 47, the position of the HAPA monolayer was varied from closest to the electrode surface (N = 1) to furthest away from the surface (N = 7). These mixed ZP films were characterized prior to the EM-SPR experiments with PM-FTIRRAS and scanning in situ SPR measurements; no significant changes in film structure, molecular orientation, or overall film thickness (17 ± 1 nm) were observed as the HAPA monolayer position was varied [105]. Figure 47 plots the change observed in the electric field strength (ΔE) obtained from the differential reflectivity curves for a potential modulation $\Delta\phi_m$ of 50 mV as a function of the position of HAPA in a sample (N). As the HAPA layer was placed further away from the electrode surface, a linear decrease in ΔE was ob-

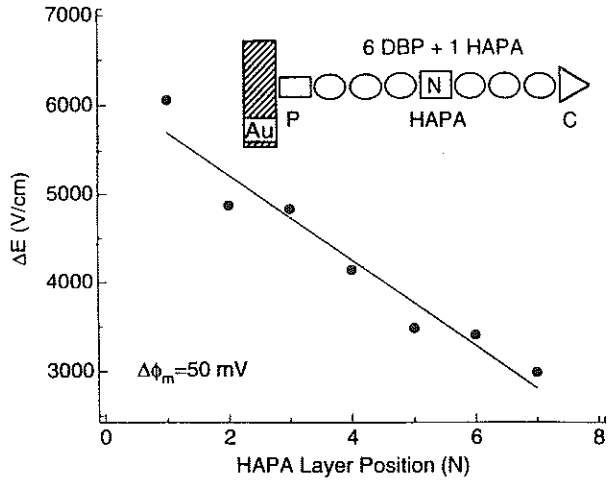

FIG. 47. The variation in the change in electric field strength (ΔE) within a 17 ± 1 nm thick multilayer ZP film that consisted of a phosphorylated MUD primer monolayer, one HAPA monolayer, six DBP monolayers, and one DHP capping monolayer. These ΔE values are obtained via changes in the EM-SPR reflectivity curves by systematically varying the position of the HAPA monolayer within the multilayer ZP film (see inset). The linear decrease in ΔE is attributed to ion and solvent penetration into the multilayer film, and implies a quadratic decrease with thickness of the local potential φ inside the ZP film. (From Ref. 105.)

served with a maximum loss of 50% at the outermost (N = 7) position. This decrease is not expected from a simple parallel-plate capacitor model of the interface, which would predict a constant electric field inside the film [171].

A number of possibilities exist to account for the observed decrease in ΔE: (1) the orientation or tilt angle of the HAPA chromophores is changing with position in the multilayer film; (2) changes in the HAPA layer packing density as a function of position in the mixed ZP films are taking place; (3) loss of noncentrosymmetry in the ZP film is due to HAPA intercalation and randomization into the DBP portions of the multilayer; (4) ion and solvent penetration occurs into the ZP multilayer resulting in a decrease in the electric field strength within the film. The PM-FTIRRAS and in situ SPR characterization measurements made on these mixed ZP films eliminate the first three possible sources to the measured decrease in ΔE; all of the data show that during the ZP film deposition process no significant changes in film uniformity, packing density, molecular orientation, or overall film thickness take place for the various multilayer films. This suggests that the experimentally measured linear decrease in ΔE is a result of ion and solvent penetration into the ZP film in the electrochemical environment. A linear decrease in ΔE implies a quadratic decrease with thickness of the local potential ϕ inside the ZP film; i.e., redox species incorporated into this ZP film at the N = 7 position would only experience 25% of the applied potential ϕ_m. The effect of the local potential on the electrochemical response of ultrathin organic films at electrode surfaces has been discussed previously [171–176,178,200,201], and the EM-SPR measurements described in this chapter provide a method for quantitation of the local electrostatic potential within these films.

3. *EM-SPR Interference Effects Within Mixed HAPA/PY-AZO Multilayers*

A final set of EM-SPR experiments demonstrates how interference effects between two different noncentrosymmetric ZP monolayers can be measured in order to establish the relative directional order of chromophores in mixed multilayers at electrode surfaces. These experiments incorporate mixed ZP films composed of the nonlinear optical chromophores HAPA and PY-AZO. In previous sections the EM-SPR differential reflectivity curves of ZP multilayers of these two chromophores were shown to be opposite in shape, and the electro-optic coefficients r_{33} for PY-AZO and

HAPA were determined to be opposite in sign. These values reflect the difference in the direction of the dipole moment of the PY-AZO molecule compared to that of the HAPA molecule as discussed in Sec. V.5.C.

As mentioned previously, the electro-optical response r from the interface can also be described as the complex surface nonlinear susceptibility $\chi^{(2)}(-\omega, \omega, 0)$. In addition to a magnitude, $\chi^{(2)}(-\omega, \omega, 0)$ also has a phase component associated with it. The phase of $\chi^{(2)}$ has been used previously in SHG experiments to ascertain the absolute orientation of a monolayer film [10]. For example, interference effects have been observed in the SHG from mixed monolayers of two similar chromophores pointing in opposite directions at a liquid/liquid interface [202]. This same type of cancellation effect should also be observable in EM-SPR experiments on mixed ZP films containing both HAPA and PY-AZO monolayers.

To demonstrate this effect, EM-SPR measurements were performed on a set of three mixed HAPA/PY-AZO multilayer films: (1) a ZP film with two PY-AZO monolayers and one HAPA monolayer, (2) a ZP film with one PY AZO monolayer and two HAPA monolayers, and (3) a ZP film with one PY AZO and one HAPA monolayer. Each of these ZP multilayers contained a phosphorylated MUD primer layer and a DHP capping monolayer; each of these ZP films was characterized with PM-FTIRRAS prior to the EM-SPR measurements. The PM-FTIRRAS spectra indicated that the HAPA and PY AZO monolayers in the mixed films had molecular structures and packing densities equivalent to those observed in pure films of the two chromophores. The EM-SPR differential reflectivity curves for these three films are shown in Figures 48 and 49. The Δ%R curve for the "1 PY-AZO + 2 HAPA" ZP film in Fig. 48a has a waveform similar to the Δ%R curve for a single HAPA monolayer, whereas the Δ%R curve for the "2 PY-AZO + 1 HAPA" sample in Fig. 48b has a waveform similar to the Δ%R curve for a single PY-AZO monolayer. The difference in the waveform for these two samples is due to the interference between the electro-optical response of the HAPA and PY AZO monolayers in the ZP films. Figure 49 plots the Δ%R curve (solid line) for the "1 PY-AZO + 1 HAPA" ZP film and shows a complete cancellation of the electro optical response of the ZP multilayer. The residual EM-SPR differential reflectivity signal observed from this sample is due to contributions from the metal substrate and is consistent with the Δ%R curves obtained from a centrosymmetric DBP ZP film of similar thickness (dashed line in Fig. 49).

These measurements are the first observation of interference effects

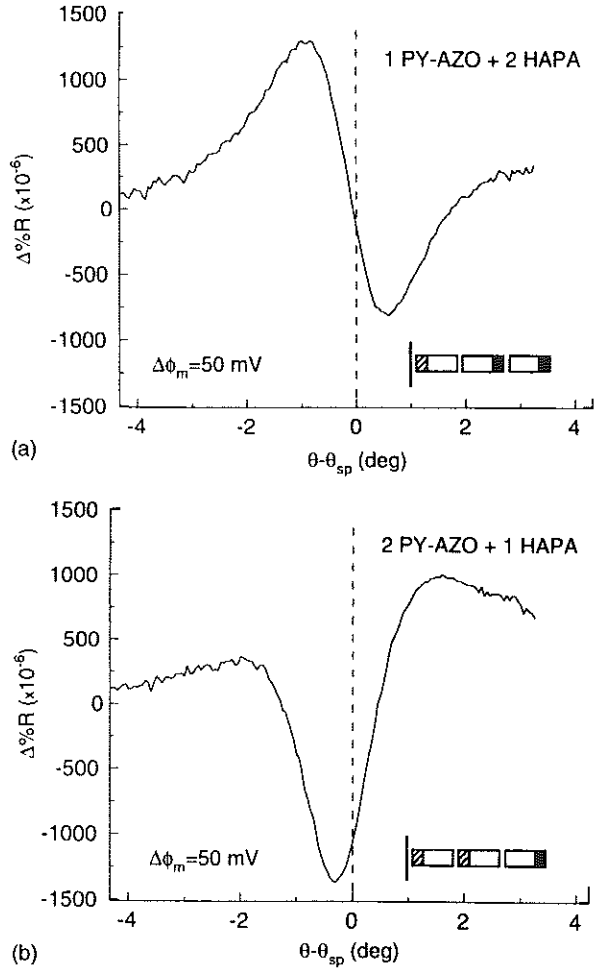

FIG. 48. Differential reflectivity (Δ%R) obtained by EM-SPR measurements for (a) a ZP film with one PY-AZO monolayer and two HAPA monolayers, 1 PY-AZO + 2 HAPA, and (b) a ZP film with two PY-AZO monolayers and one HAPA monolayer, 2 PY-AZO + 1 HAPA. Each of these ZP multilayer films contained a phosphorylated MUD primer layer and a DHP capping monolayer. The curve in (a) has the waveform of a HAPA sample, while (b) has the waveform of a PY-AZO sample. The difference in the waveform for these two samples is due to the interference between the electro-optical responses of the HAPA and PY-AZO monolayers in the ZP films. (From Ref. 105.)

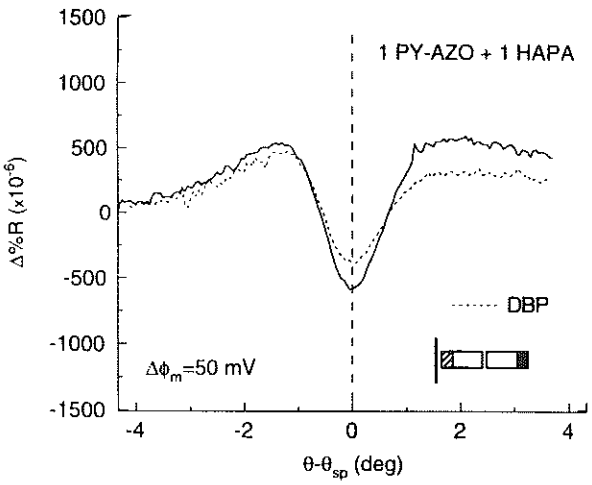

FIG. 49. Differential reflectivity (Δ%R) obtained by EM-SPR measurements for a ZP film with one PY-AZO and one HAPA monolayer, 1 PY-AZO + 1 HAPA (solid line). This ZP multilayer film also contained a phosphorylated MUD primer layer and a DHP capping monolayer. The solid curve shows a complete cancellation of the electro-optical response of the ZP multilayer. The residual EM-SPR differential reflectivity signal observed from this sample is due to contributions from the metal substrate. This substrate response is the same as that observed from a centrosymmetric DBP ZP film of similar thickness (dashed line). (From Ref. 105.)

in EM-SPR measurements on self-assembled noncentrosymmetric films and demonstrate unequivocally that mixed ZP multilayers with different oriented chromophore monolayers can be created. The amount of interference observed from the mixed ZP multilayers also depends upon the electric field profile through the ultrathin film. For example, a less pronounced interference effect was observed from a "1 HAPA + 1 PY-AZO" ZP film as compared to the "1 PY-AZO + 1 HAPA" ZP film shown in Fig. 49. Differences between these two films are due to the fact that the second ZP monolayer in these samples experiences a slightly lower local electric field strength (as expected from the results of Sec. V.E.2), which in the case of HAPA and PY-AZO happens to cancel out the slight difference in the magnitude of r_{33} for the two different chromophores.

VI. FUTURE DIRECTIONS

As demonstrated by the examples in the chapter, the SPR scanning and imaging experiments are two extremely sensitive methods for characterizing the thickness of ultrathin films on metal surfaces. When used in conjunction with other analytical techniques such as polarization modulation Fourier transform infrared reflection absorption spectroscopy, detailed information about the assembly, structure, and reactivity of adsorbed monolayer can be ascertained. For electrochemical systems, the EM-SPR measurement is a very useful tool for the elucidation of the electrostatic fields inside noncentrosymmetric films at electrode surfaces.

In general, the availability of the commercial BIACORE SPR instrument since the early 1990s has led to a large increase in the use of the SPR technique in sensor applications. In the future, SPR sensor systems based on multiple wavelength excitation and fiber-optic probes may extend this technique to the on-line monitoring of catalytic processes and other chemical reactions. In an electrochemical environment, SPR fiber-optic probes combined with techniques such as anodic stripping voltammetry have been used to detect trace metal ions with a suggested eventual detection limit in the parts per billion range [203].

Although the major use of the SPR reflectivity technique is in the area of chemical and biochemical sensor devices, a number of other possible applications exist. For example, electro-optical light modulators based on SPR methods have been proposed [102–104]. In addition, multiwavelength SPR instruments or Fourier transform SPR instruments may soon compete with commercial ellipsometers to provide simultaneous determination of the thickness and index of refraction of films deposited on metal surfaces. In the future, the application of SPR methods to other spectroscopic measurements (e.g., SHG, fluorescence, Raman scattering) appears to be a very promising area of research.

ACKNOWLEDGMENTS

The authors gratefully acknowledge the support of the National Science Foundation in these studies and would like to thank Drs. R. Georgiadis, W. Knoll, D. Kolb, and K. Krischer for preprints and reprints of their SPR papers. The authors also acknowledge T. Frutos and A. Thiel for the oligonucleotide hybridization data in Fig. 35.

REFERENCES

1. A. E. Dowrey and C. Marcott, Appl. Spectrosc. *36*:414 (1982).
2. M. J. Green, B. J. Barner, and R. M. Corn, Rev. Sci. Instrum. *62*:1426 (1991).
3. B. J. Barner, M. J. Green, E. I. Saez, and R. M. Corn, Analytical Chemistry *63*:55 (1991).
4. R. V. Duevel and R. M. Corn, Anal. Chem. *64*:337 (1992).
5. B. L. Frey, D. G. Hanken, and R. M. Corn, Langmuir *9*:1815 (1993).
6. C. E. Jordan, B. L. Frey, S. Kornguth, and R. M. Corn, Langmuir *10*:3642 (1994).
7. B. Beden and C. Lamy, in *Spectroelectrochemistry; Theory and Practice* (R. J. Gale, ed.), Plenum Press, New York, 1988.
8. B. Beden, in *Spectroscopic and Diffraction Techniques in Interfacial Electrochemistry* (C. Gutierrez and C. Melendres, eds.), Kluwer Academic Publishers, Dordrecht, The Netherlands, 1990, p. 103.
9. S. M. Stole, D. D. Popenoe, and M. D. Porter, in *Electrochemical Interfaces: Modern Techniques for In-Situ Interface Characterization* (H. D. Abruna, ed.), VCH, New York, 1991, ch. 7.
10. R. M. Corn and D. A. Higgins, Chem. Rev. *94*:107 (1994).
11. R. M. Corn and D. A. Higgins, *Characterization of Organic Thin Films*, Butterworth-Heineman, 1995.
12. Y. R. Shen, in *Spectroscopic and Diffraction Techniques in Interfacial Electrochemistry* (C. Gutierrez and C. Melendres, eds.), Kluwer Academic Publishers, Dordrecht, The Netherlands, 1990, p. 281–311.
13. C. D. Bain, J. Chem. Soc. Faraday Trans. *91*:1281 (1995).
14. P. Guyot-Sionnest, R. Superfine, J. H. Hunt, and Y. R. Shen, Chem. Phys. Lett. *144*:1 (1988).
15. T. H. Ong, R. N. Ward, P. B. Davies, and C. D. Bain, J. Am. Chem. Soc. *114*:6243 (1992).
16. T. H. Ong, P. B. Davies, and C. D. Bain, Langmuir *9*:1836 (1993).
17. D. M. Kolb, in *Spectroelectrochemistry: Theory and Practice* (R. J. Gale, ed.), Plenum Press, New York, 1988, ch. 4.
18. W. Plieth, in *Spectroscopic and Diffraction Techniques in Interfacial Electrochemistry* (C. Gutierrez and C. Melendres, eds.), Kluwer Academic Publishers, Dordrecht, The Netherlands, 1990, p. 223.
19. J. Pemberton, in *Electrochemical Interfaces: Modern Techniques for In-Situ Interface Characterization* (H. D. Abruna, ed.), VCH, New York, 1991, ch. 5.
20. R. K. Chang, in *Spectroscopic and Diffraction Techniques in Interfacial Electrochemistry* (C. Gutierrez and C. Melendres, eds.), Kluwer Academic Publishers, Dordrecht, The Netherlands, 1990, p. 155.
21. R. L. Birke and J. R. Lombardi, in *Spectroelectrochemistry: Theory and Practice* (R. J. Gale, ed.), Plenum Press, New York, 1988, ch. 6.

22. E. Burstein, W. P. Chen, Y. J. Chen, and A. Hartstein, J. Vac. Sci. Technol. *11*:1004 (1974).
23. H. Raether, in *Physics of Thin Films*, Vol. 9, Academic Press, New York, 1977, p. 145.
24. V. M. Agranovich and D. L. Mills, eds., *Surface Polaritons: Electromagnetic Waves at Surfaces and Interfaces*, North-Holland, Amsterdam, 1982.
25. H. Knobloch, C. Duschl, and W. Knoll, J. Chem. Phys. *91*:3810 (1989).
26. H. Knobloch, H. Brunner, A. Leitner, F. Aussenegg, and W. Knoll, J. Chem. Phys. *98*:10093 (1993).
27. H. Kano and S. Kawata, Optics Lett. *21*:1848 (1996).
28. S. Byahut and T. E. Furtak, Rev. Sci. Instrum. *61*:27–32 (1990).
29. B. Pettinger, A. Tadjeddine, and D. B. Kolb, Chem. Phys. Lett. *66*:544 (1979).
30. A. Girlando, M. R. Philpott, D. Heitmann, J. D. Swalen, and R. Santo, J. Chem. Phys. *72*:5187 (1980).
31. W. Knoll, M. R. Philpott, J. D. Swalen, and A. Girlando, J. Chem. Phys. *77*:2254–2260 (1982).
32. S. Ushioda and R. Loudon, in *Surface Polaritons: Electromagnetic Waves at Surfaces and Interfaces* (V. M. Agranovich and D. L. Mills, eds.), North-Holland, Amsterdam, 1982, p. 535.
33. S. Ushioda and Y. Sasaki, Phys. Rev. B *27*:1401 (1983).
34. R. M. Corn and M. R. Philpott, J. Chem. Phys. *80*:5245 (1984).
35. C. Duschl and W. Knoll, J. Chem. Phys. *88*:4062 (1988).
36. B. Rothenhäusler, C. Duschl, and W. Knoll, Thin Solid Films *159*:323 (1988).
37. J. Giergiel, C. E. Reed, J. C. Hemminger, and S. Ushioda, J. Phys. Chem. *92*:5357 (1988).
38. W. Wittke, A. Hatta, and A. Otto, Appl. Phys. A *48*:289 (1989).
39. M. G. Lee, J. H. Lee, and J. S. Chang, Surf. Sci. Lett. *271*:L362 (1992).
40. A. Nemetz, T. Fischer, A. Ulman, and W. Knoll, J. Chem. Phys. *98*:5912 (1993).
41. M. Futamata, Langmuir *11*:3894 (1995).
42. M. Futamata, J. Phys. Chem. *99*:11901 (1995).
43. M. Futamata, E. Keim, A. Bruckbauer, D. Schumacher, and A. Otto, Appl. Surf. Sci. *100/101*:60 (1996).
44. H. J. Simon, D. E. Mitchell, and J. G. Watson, Phys. Rev. Lett. 33:1531 (1974).
45. H. J. Simon, R. E. Benner, and J. G. Rako, Opt. Commun. *23*:245 (1977).
46. F. DeMartini, P. Ristori, E. Santamato, and A. C. A. Zammit, Phys. Rev. B *8*: 3797 (1981).
47. Y. R. Shen and F. DeMartini, in *Surface Polaritons: Electromagnetic Waves at Surfaces and Interfaces* (V. M. Agranovich and D. L. Mills, eds.), North-Holland, Amsterdam, 1982, p. 629.

48. J. E. Sipe and G. I. Stegeman, in *Surface Polaritons: Electromagnetic Waves at Surfaces and Interfaces* (V. M. Agranovich and D. L. Mills, eds.), North-Holland, Amsterdam, 1982, p. 661.
49. R. T. Deck and D. Sarid, J. Opt. Soc. Am. *72*:1613 (1982).
50. R. M. Corn, M. Romagnoli, M. D. Levenson, and M. R. Philpott, Chem. Phys. Lett. *106*:30 (1984).
51. P. M. Adam, L. Salomon, F. de Fornel, and J. P. Goudonnet, Phys. Rev. B *48*:2680 (1993).
52. F. Chao, M. Costa, and A. Tadjeddine, J. Electroanal. Chem. *329*:313 (1992).
53. R. M. A. Azzam and N. M. Bashara, *Ellipsometry and Polarized Light*, North-Holland, Amsterdam, 1977.
54. W. Plieth, Kozlowski, and T. Twomey, in *Adsorption of Molecules at Metal Electrodes*, Vol. 239 (J. Lipkowski and P. N. Ross, eds.), VHC, New York, 1992.
55. A. Ulman, *An Introduction to Ultrathin Organic Films*, Academic Press, New York, 1991.
56. K. A. Peterlinz and R. Georgiadis, Langmuir *12*:4731 (1996).
57. S. Löfås, M. Malmqvist, I. Rönnberg, E. Stenberg, B. Liedberg, and I. Lundström, Sensors Actuators B *5*:79–84 (1991).
58. J. Spinke, M. Liley, H.-J. Guder, L. Angermaier, and W. Knoll, Langmuir *9*:1821 (1993).
59. J. Spinke, M. Liley, F.-J. Schmitt, H. J. Guder, L. Angermaier, and W. Knoll, J. Chem. Phys. *99*:7012 (1993).
60. M. Mrksich, G. B. Sigal, and G. M. Whitesides, Langmuir *11*:4383 (1995).
61. K. A. Peterlinz, R. Georgiadis, T. M. Herne, and M. J. Tarlov, J. Am. Chem. Soc. *119*:3401 (1997).
62. I. Pockrand, J. D. Swalen, J. G. I. Gordon, and M. R. Philpott, Surf. Sci. *74*:237 (1977).
63. D. G. Hanken and R. M. Corn, Anal. Chem. *67*:3767–3774 (1995).
64. D. G. Hanken, R. R. Naujok, J. M. Gray, and R. M. Corn, Anal. Chem. *69*:240 (1997).
65. R. Kotz, D. M. Kolb, and J. K. Sass, Surf. Sci. *69*:359 (1977).
66. J. G. Gordon and S. Ernst, Surf. Sci. *101*:499 (1980).
67. A. Tadjeddine, Electrochim. Acta *34*:29 (1989).
68. D. M. Kolb, in *Surface Polaritons: Electromagnetic Waves at Surfaces and Interfaces* (V. M. Agranovich and D. L. Mills, eds.), North Holland, Amsterdam, 1982, p. 299.
69. G. Flatgen, K. Krischer, B. Pettinger, K. Doblhofer, H. Junkes, and G. Ertl, Science *269*:668 (1995).
70. X. Chen, M. C. Davies, K. M. Shakesheff, S. J. B. Tendler, P. M. Williams, and J. Davies, J. Vac. Sci. Technol. B *14*:1582 (1996).
71. J. Davies, C. J. Roberts, A. C. Dawkes, J. Sefton, J. C. Edwards, T. O. Glasbey, A. G. Haymes, M. C. Davies, D. E. Jackson, M. Lomas, K. M. Shakesh-

eff, S. J. B. Tendler, M. J. Wilkins, and P. M. Williams, Langmuir *10*:2654 (1994).
72. X. Chen, K. M. Shakesheff, M. C. Davies, J. Heller, C. J. Roberts, S. J. B. Tendler, and P. M. Williams, J. Phys. Chem. *99*:11537 (1995).
73. K. M. Shakesheff, X. Chen, M. C. Davies, A. Domb, C. J. Roberts, S. J. B. Tendler, and P. M. Williams, Langmuir *11*:3921 (1995).
74. S. I. Bozhevolnyi, B. Vohnsen, I. I. Smolyaninov, and A. V. Zayats, Optics Communications *117*:417 (1995).
75. J. D. Swalen, J. G. Gordon, M. R. Philpott, A. Brillante, I. Pockrand, and R. Santo, Am. J. Phys. *48*:669 (1980).
76. A. Otto, Z. Phys. *216*:398 (1968).
77. E. Kretschmann and H. Raether, Z. Naturforsch. Teil A *23*:2135 (1968).
78. A. Brillante and I. Pockrand, J. Mol. Struct. *79*:169 (1982).
79. A. Hatta, S. Suzuki, and W. Suetaka, Appl. Surf. Sci. *40*:9 (1989).
80. I. Pockrand, J. D. Swalen, R. Santo, A. Brillante, and M. R. Philpott, J. Chem. Phys. *69*:4001 (1978).
81. G. H. Cross, N. A. Cade, I. R. Girling, I. R. Peterson, and D. C. Andrews, J. Chem. Phys. *86*:1061 (1987).
82. K. A. Peterlinz and R. Georgiadis, Optics Commun. *130*:260 (1996).
83. K. S. Johnston, S. R. Karlsen, C. C. Jung, and S. S. Yee, Mater. Chem. Phys. *42*:242 (1995).
84. R. C. Jorgenson, C. C. Jung, S. S. Yee, and L. W. Burgess, Sensors Actuators B *13–14*:721 (1993).
85. S. R. Karlsen, K. S. Johnston, R. C. Jorgenson, and S. S. Yee, Sensors Actuators B *24–25*:747 (1995).
86. C. R. Lawrence, A. S. Martin, and J. R. Sambles, Thin Solid Films *208*:269 (1992).
87. M. A. Kessler and E. A. H. Hall, J. Colloid Interface Sci. *169*:422 (1995).
88. J. G. Gordon and J. D. Swalen, Opt. Commun. *22*:374 (1977).
89. I. Pockrand, Surf. Sci. *72*:577–588 (1978).
90. I. Pockrand and J. D. Swalen, J. Opt. Soc. Am. *68*:1147 (1978).
91. J. C. Loulergue, M. Dumont, Y. Levy, P. Robin, J. P. Pocholle, and M. Papuchon, Thin Solid Films *160*:399 (1988).
92. W. M. K. P. Wijekoon, B. Asgharian, M. Casstevens, M. Samoc, G. B. Talapatra, P. N. Prasad, T. Geisler, and S. Rosenkilde, Langmuir *8*:135 (1992).
93. D. Morichere, V. Dentan, F. Kajzar, P. Robin, Y. Levy, and M. Dumont, Optics Comm. *74*:69 (1989).
94. V. Dentan, Y. Levy, M. Dumont, P. Robin, and E. Chastaing, Optics Comm. *69*:379 (1989).
95. H. Knobloch, H. Orendi, M. Buchel, M. Sawodny, A. Schmidt, and W. Knoll, Fresenius J. Anal. Chem. *349*:107 (1994).
96. Z. Sekkat, C.-S. Kang, E. F. Aust, G. Wegner, and W. Knoll, Chem. Mater. *7*:142 (1995).

97. B. L. Frey, C. E. Jordan, S. Kornguth, and R. M. Corn, Anal. Chem. *67*:4452 (1995).
98. G. H. Cross, I. R. Girling, I. R. Peterson, N. A. Cade, and J. D. Earls, Elect. Lett. *22*:1111 (1986).
99. G. H. Cross, I. R. Girling, I. R. Peterson, N. A. Cade, and J. D. Earls, J. Opt. Soc. Am. B *4*:962 (1987).
100. M. Dumont, Y. Levy, and D. Morichere, in *Organic Molecules for Nonlinear Optics and Photonics* (J. Messier, ed.), Kluwer Academic Publishers, Dordrecht, The Netherlands, 1991, p. 461.
101. E. F. Aust and W. Knoll, J. Appl. Phys. *73*:2705 (1993).
102. E. M. Yeatman and M. E. Caldwell, Appl. Phys. Lett. *55*:613 (1989).
103. T. Okamoto, T. Kamiyama, and I. Yamaguchi, Optics Lett. *18*:1570 (1993).
104. C. Jung, S. Yee, and K. Kuhn, Appl. Optics *34*:946 (1995).
105. D. G. Hanken and R. M. Corn, Anal. Chem. *69*:3665 (1997).
106. D. G. Hanken and R. M. Corn, Isr. J. of Chem. *37*:165 (1997).
107. M. Malmqvist, Nature *361*:186 (1993).
108. P. Nilsson, B. Persson, M. Uhlen, and P. A. Nygren, Anal. Biochem. *224*:400 (1995).
109. B. Cheskis and L. P. Freedman, Biochemistry *35*:3309 (1996).
110. P. Schuck and A. P. Minton, Anal. Biochem. *240*:262 (1996).
111. P. Schuck, Biophys. J. *70*:1230 (1996).
112. F.-J. Schmitt, L. Haussling, H. Ringsdorf, and W. Knoll, Thin Solid Films *210/211*:815 (1992).
113. L. Haussling, H. Ringsdorf, F.-J. Schmitt, and W. Knoll, Langmuir *7*:1837 (1991).
114. J. R. Rahn and R. B. Hallock, Langmuir *11*:650 (1995).
115. N. J. Geddes, A. S. Martin, F. Caruso, R. S. Urquhart, D. N. Furlong, J. R. Sambles, K. A. Than, and J. A. Edgar, J. Immunol. Methods *175*:149 (1994).
116. P. T. Leung, D. Pollardknight, G. P. Malan, and M. F. Finlan, Sensors Actuators B *22*:175 (1994).
117. D. J. v.-d. -. Heuvel, R. P. H. Kooyman, J. W. Drijfhout, and G. W. Welling, Anal. Biochem. *215*:223 (1993).
118. D. Piscevic, R. Lawall, M. Vieth, M. Liley, Y. Okahata, and W. Knoll, Appl. Surf. Sci. *90*:425 (1995).
119. A. A. Kruchinin and Y. G. Vlasov, Sensors Actuators B *30*:77 (1996).
120. G. B. Sigal, C. Bamdad, A. Barberis, J. Strominger, and G. M. Whitesides, Anal. Chem. *68*:490 (1996).
121. V. I. Silin, G. A. Balcytis, G. N. Zhizhin, and V. A. Yakovlev, Vibrational Spectr. *5*:133 (1993).
122. M. Stelzle, G. Weissmuller, and E. Sackmann, J. Phys. Chem. *97*:2974 (1993).
123. S. Terrettaz, T. Stora, C. Duschl, and H. Vogel, Langmuir *9*:1361 (1993).

124. H. Lang, C. Duschl, M. Gratzel, and H. Vogel, Thin Solid Films *210/211*:818 (1992).
125. E. L. Florin and H. E. Gaub, Biophys. J. *64*:375 (1993).
126. E. Stenberg, B. Persson, H. Roos, and C. Urbaniczky, J. Colloid Interface Sci. *143*:513 (1990).
127. A. Szabo, L. Stolz, and R. Granzow, Current Opin. Struct. Biol. *5*:699 (1995).
128. B. Rothenhäusler and W. Knoll, Nature *332*:615 (1988).
129. C. E. Jordan and R. M. Corn, Anal. Chem. *69*:1449 (1997).
130. W. Hickel and W. Knoll, J. Appl. Phys. *67*:3572 (1990).
131. F.-J. Schmitt and W. Knoll, Biophys. J. *60*:716 (1991).
132. B. Fischer, S. P. Heyn, M. Egger, and H. E. Gaub, Langmuir *9*:136 (1993).
133. J. S. Schildkraut, Appl. Optics *27*:3329 (1988).
134. H. E. de Bruijn, B. S. F. Altengurg, R. P. H. Kooyman, and J. Greve, Optics Commun. *82*:425 (1991).
135. H. E. de Bruijn, M. Minor, R. P. H. Kooyman, and J. Greve, Optics Commun. *95*:183 (1993).
136. E. D. Palik, ed., *Handbook of Optical Constants of Solids*, Academic Press, Orlando, 1985.
137. M. D. Porter, D. L. Allara, T. B. Bright, and C. E. D. Chidsey, J. Am. Chem. Soc. *109*:3559 (1987).
138. C. A. Goss, D. H. Charych, and M. Majda, Anal. Chem. *63*:85 (1991).
139. T. Hoshi, J. Anzai, and T. Osa, Anal. Chem. *67*:770 (1995).
140. N. M. Green, in *Advances in Protein Chemistry*, Academic Press, New York, 1975, p. 85.
141. L. Pugliese, A. Coda, M. Malcovati, and M. Bolognesi, J. Mol. Biol. *231*:698 (1993).
142. M. Wilchek and E. A. Bayer, Anal. Biochem. *171*:1 (1988).
143. R. C. Ebersole, J. A. Miller, J. R. Moran, and M. D. Ward, J. Am. Chem. Soc. *112*:3239 (1990).
144. S. Zhao and W. M. Reichert, Langmuir *8*:2785 (1992).
145. P. M. Nellen and W. Lukosz, Biosensors Bioelectronics *8*:129 (1993).
146. P. Pantano and W. G. Kuhr, Anal. Chem. *65*:623 (1993).
147. G. Decher, B. Lehr, K. Lowack, Y. Lvov, and J. Schmitt, Biosensors Bioelectronics *9*:677–648 (1994).
148. M. S. Ayyagari, R. Pande, S. Kamtekar, H. Gao, K. A. Marx, J. Kumar, S. K. Tripathy, J. A. Akkara, and D. L. Kaplan, Biotechnol. Bioeng. *45*:116 (1995).
149. H. Morgan, D. M. Taylor, and C. D'Silva, Thin Solid Films *209*:122 (1992).
150. K. Fujita, S. Kimura, Y. Imanishi, E. Rump, J. van Esch, and H. Ringsdorf, J. Am. Chem. Soc. *116*:5479 (1994).
151. R. M. Zimmerman and E. C. Cox, Nucleic Acids Res. *22*:492 (1994).

152. C. D. Bain, E. B. Troughton, Y.-T. Tao, J. Evall, G. M. Whitesides, and R. G. Nuzzo, J. Am. Chem. Soc. *111*:321 (1989).
153. C. E. D. Chidsey and D. N. Loiacono, Langmuir *6*:682 (1990).
154. E. L. Smith, C. A. Alves, J. W. Anderegg, M. D. Porter, and L. M. Siperko, Langmuir *8*:2707 (1992).
155. L. Sun, R. M. Crooks, and A. J. Ricco, Langmuir *9*:1775 (1993).
156. S. J. Stranick, A. N. Parikh, Y.-T. Tao, D. L. Allara, and P. S. Weiss, J. Phys. Chem. *98*:7636 (1994).
157. J. P. Folkers, P. E. Laibinis, and G. M. Whitesides, Langmuir *8*:1330 (1992).
158. O. Chailapakul and R. M. Crooks, Langmuir *9*:884 (1993).
159. H. Lee, H. G. Hong, T. E. Mallouk, and L. J. Kepley, J. Am. Chem. Soc. *110*:618 (1988).
160. H. Lee, T. E. Mallouk, L. J. Kepley, H. G. Hong, and S. Akhter, J. Phys. Chem. *92*:2597 (1988).
161. H. C. Yang, K. Aoki, H.-G. Hong, D. D. Sackett, M. F. Arendt, S.-L. Yau, C. M. Bell, and T. E. Mallouk, J. Am. Chem. Soc. *115*:11855 (1993).
162. T. M. Putvinski, M. L. Schilling, H. E. Katz, C. E. D. Chidsey, A. M. Mujsce, and A. B. Emerson, Langmuir *6*:1567 (1990).
163. A. C. Zeppenfeld, S. L. Fiddler, W. K. Ham, B. J. Klopfenstein, and C. J. Page, J. Am. Chem. Soc. *116*:9158 (1994).
164. M. B. Dines and P. M. DiGiacomo, Inorganic Chem. *20*:92 (1981).
165. W. Kohler, D. R. Robello, C. S. Willand, and D. J. Williams, Macromolecules *24*:4589 (1991).
166. J. Huang, D. A. Dahlgren, and J. C. Hemminger, Langmuir *10*:626 (1994).
167. M. J. Tarlov, D. R. F. Burgess, and G. Gillen, J. Am. Chem. Soc. *115*:5305 (1993).
168. D. Piscevic, W. Knoll, and M. J. Tarlov, Supramol. Sci. *2*:99 (1995).
169. C. E. Jordan, A. G. Frutos, A. J. Thiel, and R. M. Corn, Anal. Chem. *69*:4939 (1997).
170. A. Frutos, Q. Liu, A. Thiel, A. M. W. Sanner, A. E. Condon, L. M. Smith, and R. M. Corn, Nucleic Acids Res. *25*:4748 (1997).
171. A. J. Bard and L. R. Faulkner, *Electrochemical Methods*, J. Wiley, New York, 1980.
172. H. O. Finklea, in *Electroanalytical Chemistry: A Series of Advances*, Vol. 19 (A. J. Bard and I. Rubinstein, eds.), Marcel Dekker, Inc., New York, 1996, p. 109.
173. C. P. Smith and H. S. White, Anal. Chem. *64*:2398 (1992).
174. C. P. Smith and H. S. White, Langmuir *9*:1 (1993).
175. W. R. Fawcett, M. Fedurco, and Z. Kovacova, Langmuir *10*:2403 (1994).
176. W. R. Fawcett, J. Electroanal. Chem. *378*:117 (1994).
177. P. H. Schmidt and W. J. Plieth, J. Electroanal. Chem. *201*:163 (1986).
178. C. A. Widrig, C. Chung, and M. D. Porter, J. Electroanal. Chem. *201*:335 (1991).

179. J. M. Pope, Z. Tan, S. Kimbrell, and D. A. Buttry, J. Am. Chem. Soc. *114*:10085 (1992).
180. J. M. Pope and D. A. Buttry, in press.
181. D. J. Lockhart and S. G. Boxer, Chem. Phys. Lett. *144*:243 (1988).
182. D. J. Lockhart, C. Kirmaier, D. Holten, and S. G. Boxer, J. Phys. Chem. *94*:6987 (1990).
183. S. E. Creager and K. Weber, Langmuir *9*:844 (1993).
184. G. K. Rowe and S. E. Creager, J. Phys. Chem. *98*:5500 (1994).
185. X. Gao, H. S. White, S. Chen, and H. D. Abruna, Langmuir *11*:4554 (1995).
186. Y. R. Shen, *The Principles of Nonlinear Optics*, Wiley, New York, 1984.
187. K. D. Singer, S. L. Lalama, J. E. Sohn, and R. D. Small, in *Nonlinear Optical Properties of Organic Molecules and Crystals*, Vol. 1 (D. S. Chemla and J. Zyss, eds.), Academic Press, Orlando, 1987, p. 437.
188. K. D. Singer, M. G. Kuzyk, and J. E. Sohn, J. Opt. Soc. Am. B *4*:968 (1987).
189. D. R. Robello, P. T. Dao, J. Phelan, J. Revelli, J. S. Schildkraut, M. Scozzafava, A. Ulman, and C. S. Willand, Chem. Mater. *4*:425 (1992).
190. D. R. Robello, P. T. Dao, J. S. Schildkraut, M. Scozzafava, E. J. Urankar, and C. S. Willand, Chem. Mater. *7*:284 (1995).
191. H. E. Katz, G. Scheller, T. M. Putvinski, M. L. Schilling, W. L. Wilson, and C. E. D. Chidsey, Science *254*:1485 (1991).
192. H. E. Katz, W. L. Wilson, and G. Scheller, J. Am. Chem. Soc. *116*:6636 (1994).
193. H. E. Katz and M. L. Schilling, Chem. Mater. *5*:1162 (1993).
194. R. R. Naujok, D. A. Higgins, D. G. Hanken, and R. M. Corn, J. Chem. Soc., Faraday Trans.:1411 (1995).
195. D. M. Burland, R. D. Miller, and C. A. Walsh, Chem. Rev. *94*:31 (1994).
196. M. Ahlheim, M. Barzoukas, P. V. Bedworth, M. Blanchard-Desce, A. Fort, Z.-Y. Hu, S. R. Marder, J. W. Perry, C. Runser, M. Staehelin, and B. Zysset Science *271*:335 (1996).
197. T.-A. Chen, A. K.-Y. Jen, and Y. Cai, J. Am. Chem. Soc. *117*:7295 (1995).
198. T. Verbiest, D. M. Burland, M. C. Jurich, V. Y. Lee, R. D. Miller, and W. Volksen, Science *268*:1604 (1995).
199. L. J. Kepley, D. D. Sackett, C. M. Bell, and T. E. Mallouk, Thin Solid Films *208*:132 (1992).
200. S. D. Evans and A. Ulman, Chem. Phys. Lett. *170*:462 (1990).
201. A. M. Becka and C. J. Miller, J. Phys. Chem. *97*:6233 (1993).
202. D. A. Higgins, R. R. Naujok, and R. M. Corn, Chem. Phys. Lett. *213*:485 (1993).
203. C. C. Jung, S. B. Saban, S. S. Yee, and R. B. Darling, Sensors and Actuators B *32*:143 (1996).
204. B. L. Frey, Ph.D Thesis, University of Wisconsin, Madison, 1996.